UCLouvain

École polytechnique de Louvain

Numerical Modelling of the Fluid–Structure Interaction of a MOSE-Inspired Storm Surge Barrier Using PFEM

Author: **Louise VERSCHUERE**
Supervisors: **Vincent LEGAT, Jonathan LAMBRECHTS**
Readers: **Michel HENRY, Sandra SOARES FRAZAO**
Academic year 2025–2026
Master [120] in Mechanical Engineering

This thesis used AI-based tools (ChatGPT, Claude, Copilot) to assist with rephrasing, language editing and the implementation of parts of the simulation code.

Abstract

The city of Venice is increasingly exposed to flooding, driven by land subsidence and a climate-amplified sea-level rise. Its MOSE storm surge barrier relies on bottom-hinged gates that are raised by compressed-air injection to isolate the lagoon from the Adriatic Sea during *acqua alta* events. This thesis models the fluid–structure interaction of a MOSE-inspired gate using the Particle Finite Element Method (PFEM), a Lagrangian approach well suited to large free-surface deformations.

The gate is first deployed under a prescribed angular velocity, then coupled to the fluid. The loading is dominated by pressure, while the vorticity field reveals local flow separation and recirculation. In the coupled case, the gate motion emerges from a torque balance and settles around an equilibrium angle 32°. The coupling is stabilized with a relaxation technique and an added-mass correction. A final, preliminary simulation confirms that the model can handle wave loading.

Acknowledgments

Ce mémoire s'est révélé être un défi à bien des égards mais également une expérience particulièrement enrichissante.

J'ai beaucoup apprécié l'opportunité de travailler sur un projet mêlant deux échelles très différentes de l'ingénierie. D'un côté, une problématique très concrète, les inondations, la protection des zones côtières et l'impact croissant des changements climatiques. De l'autre, les méthodes numériques, notamment les PFEM et le projet *MigFlow*, qui permettent d'explorer les phénomènes physiques dans leurs moindres détails, jusqu'à l'imposition d'équations décrivant, par exemple, l'existence d'une bulle. Cette diversité d'approches m'a permis de découvrir des aspects de l'ingénierie que je ne connaissais pas et a nourri ma curiosité durant ce projet.

Je tiens à remercier toute l'équipe avec laquelle j'ai eu l'occasion de travailler : Vincent Legat, Jonathan Lambrechts, Michel Henry, Alexandre Pirot et James Gosselet. Merci pour votre disponibilité, vos conseils et votre encadrement au long de cette année.

Je souhaite également remercier les autres mémorants que j'ai eu le plaisir de rencontrer dans le local visiteurs du bâtiment Euler.

Enfin, un immense merci à mes amis et à ma famille pour leur soutien, qui a très certainement contribué à l'aboutissement de ce travail !

Contents

Introduction **1**

1 Coastal Flood Protection: From Physical Mechanisms to the MOSE System **2**

1.1 Context 2
1.1.1 Land Subsidence and Sea-Level Rise 2
1.1.2 The City and Lagoon of Venice 4
1.1.3 Protecting the Lagoon's Future 5
1.2 Hydrodynamic Processes Governing Water Levels in the Venice Lagoon 5
1.2.1 Tides 6
1.2.2 Storm Surges 9
1.2.3 Seiches 9
1.3 Coastal Flooding and Mitigation Strategies 11
1.4 Storm Surge Barriers 14
1.5 The MOSE System 16
1.5.1 Operating Principle 16
1.5.2 Performance and Longtime Effectiveness 18
1.5.3 Engineering and Operational Challenges 18
1.6 Summary and Transition 19

2 The Particle Finite Element Method **20**

2.1 Iterative Algorithm and Procedure 21
2.2 Mesh Generation and Adaptivity 22
2.3 Governing Equations 26
2.4 Advection 28
2.5 Boundary Conditions 28
2.5.1 Solid Wall Boundary Conditions 28

2.5.2 Inlet/Outlet Boundary Condition 30
2.5.3 Free Surface Boundary Conditions 30
2.5.4 Bubble Boundary Conditions 31
2.6 Stability : LBB Condition and PSPG 31

3 From Passive to Active Regime by Imposed Angular Velocity 34
3.1 Problem Description & Simplifying Assumptions 34
3.2 Simulation 1 — Prescribed Angular Velocity 36
3.2.1 Problem Setup 36
3.2.2 Results 39

4 A Torque Coupling 48
4.1 Fluid-Structure Interaction Review 48
4.1.1 Monolithic vs Partitioned Approaches 48
4.1.2 Added-Mass Effects 50
4.1.3 Coupling Strategies 51
4.2 Simulation 2 —– Buoyancy-Driven Dynamics 52
4.2.1 Problem Setup 52
4.2.2 First Attempt : Constant Motor Torque 54
4.2.3 Buoyancy-Driven Configuration 56
4.2.4 Second Attempt : Buoyancy-Driven Torque 57
4.2.5 Results 59
4.3 Simulation 3 — Wave Interaction 61
4.3.1 Problem Setup 61
4.3.2 Results 63

Conclusion 67

Bibliography 73

Introduction

In November 2019, Venice experienced its worst flooding in over 50 years, with water levels peaking at 187 cm and submerging 80 % of the city. It caused millions of euros in damage to its architectural heritage [20]. Beyond their physical damage, floodings threaten the artistic, cultural, environmental, and economic assets of one of the world's most iconic cities.

While exceptional in its intensity, this event was not an anomaly but the manifestation of a structural and growing vulnerability. Over the last century, the frequency of flooding in Venice has steadily increased due to the combined effect of relative sea level rise driven mainly by climate change and of land subsidence [34].

In response to this growing threat, the Italian government commissioned the construction of a structural protection system for the Venice Lagoon. This led to the development of the MOSE (Modulo Sperimentale Elettromeccanico or Experimental Electromechanical Module) system, a storm surge barrier designed to prevent floodwaters from entering the lagoon. The system consists of a series of flap gates, hinged at the seabed, which are raised when tidal forecasts predict water levels exceeding a defined threshold.

From an engineering standpoint, the system involves complex physical phenomena, particularly in terms of wave action and its interaction with the gates. To this end, the present work proposes to model the fluid-structure interaction governing the behavior of the MOSE system using the Particle Finite Element Method (PFEM). PFEM is a numerical approach that combines Lagrangian particle tracking with adaptive remeshing. It allows the mesh to follow the motion of fluid particles and accurately capture large free-surface deformations. The numerical model developed in this work is implemented within the *MigFlow* software environment [5] [1].

This thesis is organized as follows. The first chapter provides the background on hydrodynamic phenomena in the Venice Lagoon, the concept of storm surge barriers, and the specific characteristics of the MOSE system that will be modelled. The second chapter describes the Particle Finite Element Method. The third chapter applies it to the gate deployment under an imposed angular velocity, characterizing the resulting hydrodynamic loads. Finally, the fourth chapter introduces the fluid–structure interaction (FSI) coupling and studies the free response of the gate.

[1] MigFlow project website: `https://www.migflow.be/`.

Chapter 1

Coastal Flood Protection: From Physical Mechanisms to the MOSE System

This chapter establishes the physical and engineering foundations needed to understand the MOSE system, the reference case for this thesis. It first details the physical mechanisms behind Venice's flood vulnerability, then the engineering response that the MOSE system represents.

1.1 Context

As outlined in the introduction, Venice faces a growing flood risk driven by the combined effect of land subsidence and relative sea-level rise. These phenomena have steadily increased the frequency and severity of *acqua alta* events over the past century.

1.1.1 Land Subsidence and Sea-Level Rise

Land subsidence can be defined as the sinking of the ground surface. It results from two distinct processes operating at very different timescales, millions to thousands of years for the natural component, and decades for the anthropogenic cause. The natural subsidence is driven by geological phenomena (tectonic setting of Venice and progressive compaction of sediments). This process contributes at rates between 0.5

and 1.6 $mm/year$ depending on the period considered. The anthropogenic subsidence was caused by intensive groundwater extraction to supply Venetian industries during the mid-twentieth century. This process operated on a much shorter timescale but with larger effects. It reached rates of up to 17 $mm/year$ locally. Following regulatory intervention, groundwater pumping was drastically reduced after 1970 and large-scale anthropogenic subsidence has since ceased [38].

Sea-level changes are characterized through the Mean Relative Sea Level (RSL). It is the change in local sea level measured relative to the local solid surface, as recorded by tide gauges. In Venice, the standard reference datum is the Zero Mareografico Punta della Salute (ZMPS). The ZMPS is defined as the water level recorded at the Punta della Salute tide gauge. Over the past 150 years, Venice has experienced an average RSL rise of approximately 2.5 $mm/year$ (from equal contributions of land subsidence and eustatic sea-level rise). After correction for subsidence effects, the eustatic component alone is estimated at $1.23 \pm 0.13\, mm/year$ [38].

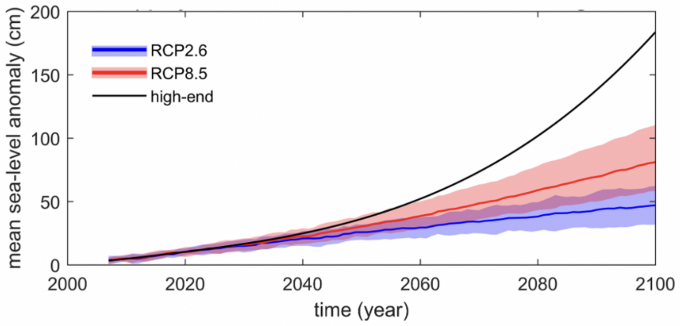


Figure 1.1: Projected northern Adriatic RSL anomalies and associated uncertainties related to socio-economic scenarios (shading: 5th–95th percentile range; line: median).[38]

However, a higher rate of sea-level rise is observed for more recent years. Between 1993 and 2019, the subsidence-corrected rate reaches $2.76 \pm 1.75\ mm/year$. Looking ahead, projections for the northern Adriatic under the RCP 8.5 high-emissions scenario suggest an additional RSL rise between 58 and 110 cm by 2100 (see Figure 1.1). It should be interpreted with caution given the large statistical uncertainties in sea-level trend estimates and the dependence on socioeconomic emissions scenarios whose future trajectory remains unknown.

1.1.2 The City and Lagoon of Venice

The Venice Lagoon (see Figure 1.2) is located at the northwestern end of the Adriatic Sea. It extends more than 60 km from north to south and approximately 12–16 km from west to east [23]. It is connected to the sea through three inlets (Lido, Malamocco and Chioggia) with widths ranging from 500 to 1000 m and depths from 7 to 13 m. For each tidal cycle, the water exchanged through the inlets is about a third of the total volume of the lagoon [23]. The lagoon is shallow, averaging 1.5 m depth, with deep tidal channels cutting through the shallower parts [34].

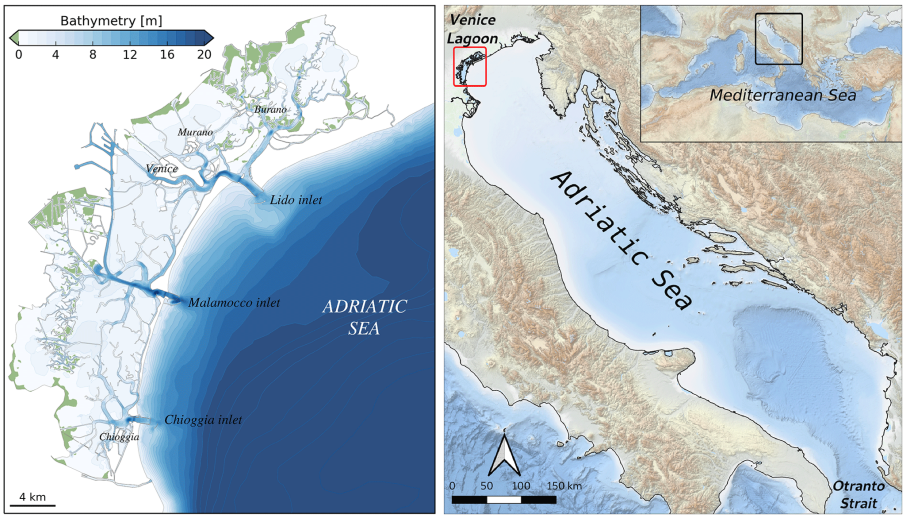


Figure 1.2: Setting of the Venice Lagoon and the Adriatic Sea.[34]

Salt marshes (*barene*) cover around 15 % of the total area and constitute a distinctive ecological feature of the lagoon. They support rich aquatic biodiversity, contribute to sediment deposition and water level regulation. Lying at an average elevation, slightly above mean sea level, they are flooded during high tides. It makes them particularly sensitive to sea-level rise and increasingly threatened by wave erosion, boat traffic, and rising sea levels [2].

Regarding tidal propagation, the tidal wave travels mainly along the deep channels before expanding into the shallower areas. Neither damping nor amplification occurs as the wave propagates inland [34]. Over the last 500 years, major engineering works have been carried out inside the lagoon, including river diversions and dredging of existing and new artificial channels. Some of these interventions are responsible for the amplification of the *acqua alta* phenomenon (see *levee effect* in Section 1.3) [34].

1.1.3 Protecting the Lagoon's Future

The catastrophic flood of 1966 marked a turning point in the perception of Venice's vulnerability. In response, the Italian government, supported by the scientific community and international organizations including UNESCO, enacted dedicated legislation to protect the lagoon from flooding, erosion, and water pollution. This culminated in the design and construction of the MOSE system (*Modulo Sperimentale Elettromeccanico*). It consists of a set of 78 independent mobile flap gates distributed across the three lagoon inlets, capable of temporarily isolating the lagoon from the Adriatic Sea during extreme surge events [23].

Extreme flooding events in Venice result from the superposition of several meteorological and oceanographic factors in the Adriatic basin. Since the MOSE gates require several hours to be raised, accurate and timely forecasting of water levels is essential for effective barrier operation [34].

Understanding the physical processes that drive water level variations in the lagoon is therefore a prerequisite for both the design and the operation of the MOSE system.

1.2 Hydrodynamic Processes Governing Water Levels in the Venice Lagoon

The total water level in Venice results from the superposition of several hydrodynamic processes as illustrated in Figure 1.3. The astronomical tide provides the baseline oscillation, while meteorological forcing (wind and atmospheric pressure) generates an additional surge component. When these contributions combine, water levels can exceed critical thresholds, giving rise to the phenomenon locally known as *acqua alta*. A tidal peak exceeding +140 cm above mean sea level is considered an extreme high water event. At this point approximately 50% of the city is flooded [26]. The following sections detail each of these contributions and the role of seiches as a persistent amplifying factor.

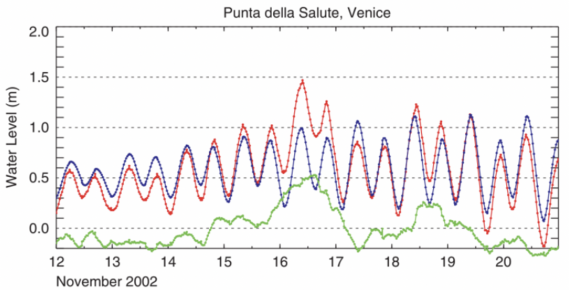


Figure 1.3: Observed (red), tidal (blue) and meteorological (green) variations of sea level [27]

1.2.1 Tides

Tides (also referred to as *gravitational* or *astronomical* tides) are defined as periodic movements directly related in amplitude and phase to geophysical forcing. The dominant geophysical forcing function is the periodic variation of the gravitational field at the Earth's surface, caused by the regular relative motions of the Moon-Earth and the Sun-Earth systems [27].

Tidal patterns are commonly classified according to their dominant period. A semidiurnal tide completes two full cycles per day, with each cycle occupying roughly half a day. The tidal range (the difference between high and low water) varies over a 14 day interval known as the spring-neap cycle (see Figure 1.4). Spring tides occur at full and new moon, when the gravitational forces of the Sun and Moon are aligned, producing a maximum tidal range [27]. Neap tides occur at the Moon's first and last quarters resulting in a minimum range. In the northern Adriatic Sea, tidal dynamics are particularly pronounced, with spring tidal ranges exceeding 1 m , sufficient to flood parts of Saint Mark's Square without any meteorological contribution [34].

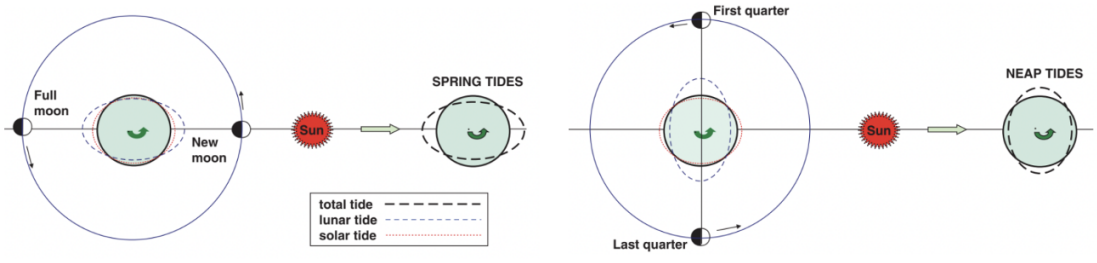


Figure 1.4: Spring and neap tides [27].

Harmonic Decomposition

Real tides result from the superposition of multiple periodic components, each associated with a specific astronomical cycle. This leads to the harmonic decomposition of the sea surface elevation $\eta(t)$:

$$\eta(t) = \sum_i A_i \cos(\omega_i t + \phi_i) \tag{1.1}$$

where A_i, ω_i and ϕ_i are respectively the amplitude, angular frequency and phase of each constituent. The main tidal constituents relevant to the northern Adriatic are listed in Table 1.1.

The tidal form factor is defined as the ratio of the amplitudes of the major diurnal and semidiurnal tidal constituents. It reveals that the semidiurnal tidal regime ($F < 1$) prevails in the Adriatic Sea [34]. It can also be observed in Figure 1.3, where two tidal cycles per day are clearly visible. A diurnal regime corresponds to $F > 3$.

Name	**Type**	**Origin**	**Amplitude [cm]**
M2	Semidiurnal	Principal lunar	23
S2	Semidiurnal	Principal solar	14
K1	Diurnal	Declinational lunisolar	16
N2	Semidiurnal	Larger elliptical lunar	[1;10]
K2	Semidiurnal	Declinational lunisolar	[1;10]
O1	Diurnal	Principal lunar	[1;10]
P1	Diurnal	Principal solar	[1;10]

Table 1.1: Main tidal constituents contributing to sea surface elevation in the northern Adriatic Sea [34][27][20].

Tidal Propagation in the Venice Lagoon

The tidal regime in the Adriatic Sea results from co-oscillations with the Mediterranean Sea, forced through the Strait of Otranto (see Figure 1.2) and amplified by resonance along the basin's longitudinal axis from south to north [34].

Tidal waves propagate as shallow water waves, since their wavelength λ is several orders of magnitude larger than the water depth h, satisfying $kh \ll 1$.

Under this condition, the general dispersion relation:

$$c^2 = \frac{g}{k}\tanh(kh) \tag{1.2}$$

reduces to:

$$c = \sqrt{gh} \tag{1.3}$$

Where c is the wave celerity and $k = \frac{2\pi}{\lambda}$ the wave number. As c is independent of k, all wavelengths propagate at the same speed, and the wave is therefore non-dispersive [8]. This result can be derived independently from the shallow water equations (Saint-Venant equations). Under the hydrostatic pressure assumption, valid when vertical accelerations are negligible compared to horizontal ones, i.e. when $\lambda \gg h$, linearized 1D equations governing the motion of a water column read:

$$\frac{\partial u}{\partial t} = -g\frac{\partial \eta}{\partial x} \qquad \text{(momentum)} \tag{1.4}$$

$$\frac{\partial \eta}{\partial t} = -h\frac{\partial u}{\partial x} \qquad \text{(continuity)} \tag{1.5}$$

where u is the depth-averaged horizontal velocity and η the free surface elevation [8]. Differentiating equation (1.4) with respect to x and equation (1.5) with respect to t, and combining:

$$\frac{\partial^2 \eta}{\partial t^2} = c^2\frac{\partial^2 \eta}{\partial x^2} \tag{1.6}$$

This is the classical *wave equation*, whose solutions are progressive waves traveling at celerity $c = \sqrt{gh}$, consistent with the shallow water limit of the dispersion relation [8].

For the Venice Lagoon ($h \approx 1.5\,m$), this gives $c \approx 3.8\,m/s$. In practice, tidal propagation in the shallow Venice Lagoon results from a balance between this wave celerity, the inertia of the water mass, and dissipative friction forces. At present, the lagoon operates close to resonance conditions. The incoming tidal wave is amplified as it propagates from the inlets toward the center [34].

1.2.2 Storm Surges

A storm surge is an anomalous rise in water level caused by meteorological forcing. At the Venetian coast, they result from wind setup and the inverse barometer effect. The wind stress contributes up to ten times more than the pressure effect alone. Storm surges in the Adriatic have been extensively studied, with particular focus on forecasting methods[20].

Wind Setup

Wind setup is defined as the change in water level induced by wind blowing over a body of water. Although the wind shear stress is locally small, its cumulative effect, when integrated over a large body of water, can be significant [8].

The Adriatic Sea is characterized by two dominant wind regimes. The sirocco is a warm, humid and southeasterly wind, associated with low-pressure systems in the northwestern Mediterranean or in the Tunisia–Sicily channel. It blows along the whole length of the Adriatic basin at typical speeds of 10–15 m/s. It causes high waves and rain and pushes water toward the closed northern end of the basin. It is the primary meteorological driver of flooding in Venice [34]. The bora is a cold, dry, northeasterly wind, reaching gusts of up to 200 km/h in the northern Adriatic. Although intense, its orientation is less aligned with the basin axis than the sirocco, resulting in different coastal impacts [34].

Low Pressure Systems

A low-pressure system creates a pressure anomaly at the ocean surface. The sea behaves as an inverted barometer, where atmospheric pressure is low, the sea surface rises. In the Adriatic basin, Mediterranean cyclones are the primary driver of this effect. They form in the northwestern Mediterranean through the interaction between atmospheric fronts and the Alpine orography. Then they track eastward over the Adriatic. When such a cyclone passes over or north of the Adriatic, it combines the inverse barometer effect with the sirocco wind, producing severe storm surge events in Venice [34].

1.2.3 Seiches

Seiches are standing waves that develop in enclosed or semi-enclosed water bodies. The Adriatic Sea behaves as a semi-enclosed basin with a node at the open southern

boundary (Strait of Otranto) and an antinode at the northern shore (Venice) [20]. A standing wave results from the superposition of two progressive waves of equal amplitude traveling in opposite directions [8]:

$$\eta(x,t) = \frac{H}{2}\cos(kx - \omega t) + \frac{H}{2}\cos(kx + \omega t) = H\cos(kx)\cos(\omega t) \tag{1.7}$$

At the open boundary, the free surface condition imposes $\eta(L,t) = 0 \,\forall\, t$, which requires [8]:

$$\cos(kL) = 0 \implies kL = \frac{(2n-1)\pi}{2} \tag{1.8}$$

This yields the Merian formula giving the natural periods of oscillations of a semi-enclosed basin [8]:

$$T_n = \frac{4L}{(2n-1)\sqrt{gh}} \tag{1.9}$$

where n=1,2,3... are the mode number. The fundamental mode (n=1) corresponds to a single oscillation over the basin length. A helpful analogy to understand this, is the sloshing of water in a bathtub. A single push sets the water oscillating at the basin's natural frequency.

For the Adriatic basin, the periods of the two fundamental modes are estimated at approximately 21h20 and 10h48 [34]. This is close to the diurnal and semidiurnal tidal periods and it partly explains the strong tidal response in the northern Adriatic.

As summarized in Figure 1.5, seiches in the Adriatic typically develop in the wake of a storm surge when the water accumulation in the northern Adriatic ceases to be supported by the wind stress. The seiches are slowly damped with a decay time of 3.2 days due to a weak frictional dissipation inside the basin and a small energy loss to the Mediterranean Sea [20].

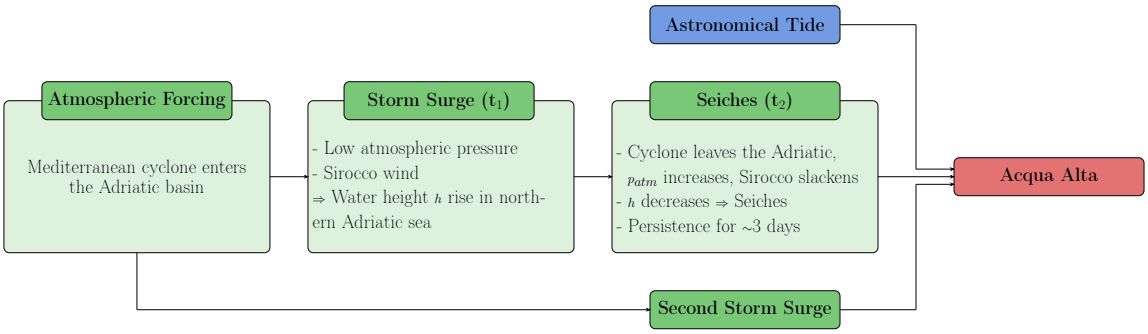


Figure 1.5: Mechanisms leading to Acqua Alta

As visible in scheme 1.5, storm surges and seiches in the Adriatic represent two distinct phases of the ocean response to atmospheric forcing. The first phase (t_1) corresponds to the wind and pressure driven storm surge, while the second phase (t_2) describes the subsequent basin relaxation through seiches after the cyclone passage.

If a successive storm surge develops before the previous seiches have fully dissipated, constructive or destructive interference may occur, depending on their relative phase [20]. In addition, the phase of the astronomical tide during these events can further modulate the resulting sea level. This can lead to acqua alta condition.

1.3 Coastal Flooding and Mitigation Strategies

Flood Risk and Human-Flood Interactions

Flood risk results from the combined effect of hazard , exposure, and vulnerability. Human societies continuously attempt to alter one or more of these factors. This creates a coupled human-flood system in which modifying one component may trigger feedback mechanisms affecting the others, sometimes with unexpected consequences [1].

The historical development of the Netherlands illustrates this dynamic particularly well. Dutch society has undergone several paradigm shifts in its relationship with flood risk. Early populations adopted a coping strategy aimed at minimizing exposure (e.g. living on higher constructed grounds). Population growth and increasing socioeconomic needs (infrastructure, transportation, and agricultural land) progressively drove a transition toward a flood protection strategy focused on minimizing hazard. This shift was further accelerated by necessity, as peat extraction caused significant land subsidence, thereby increasing flood risk. More recently, a combination of societal enrichment, scientific progress, and democratic pressure has driven a further paradigm shift, both in the Netherlands and elsewhere. With increased awareness of climate change and the accelerated sea-level rise (SLR), the perception of nature's role evolved, leading to the adoption of more integrated approaches that incorporate soft protection measures where applicable [36].

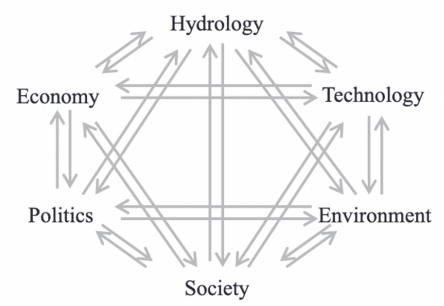


Figure 1.6: Human-flood interactions system components [1]

Another phenomenon arising from the complexity of human-flood interactions is the so-called *levee effect*. Flood protection measures can paradoxically worsen the problem they seek to address. The construction of levees fosters a false sense of security. It encourages more people to settle in flood-prone areas. Should the protection infrastructure fail, the resulting damage may far exceed what would have occurred in its absence [1].

These examples highlight that effective flood risk management requires a transdisciplinary approach, in which scientists and practitioners systematically examine the full range of interactions between system components, across natural, technical, and social dimensions [1]. Traditional coastal defense strategies can no longer be assumed as the only possible response in areas increasingly exposed to sea-level rise. A balanced mix of non-structural and structural measures based on sound scientific knowledge is essential to maintain ecological, economic, and social functions of coastal zones under changing climatic conditions [26]. Among these structural measures, coastal engineering plays a central role, constituting one of the core disciplines within this broader response.

Finally, it is important to acknowledge that flood risk is not borne equally across society. Flood vulnerability is structurally tied to economic inequality, as wealthier societies can afford protection measures that enable further development, while poorer economies remain trapped in a cycle of repeated flood damage and insufficient capital to invest in resilience [1].

Coastal Engineering and Shore Protection

Coastal engineering is a specialized branch of civil engineering focused on the design and management of structures and systems to address challenges related to coastal areas (coastal erosion, sea-level rise, storm surges, flooding, protection of valuable coastal assets and ecosystems, etc.). Beyond shore protection, coastal engineering also encompasses the design of harbors and marinas, as well as water quality management and pollutant dispersion. As illustrated in Figure 1.7, coastal systems are inherently complex. It involve multiple interacting physical processes that must all be accounted for in any engineering intervention.

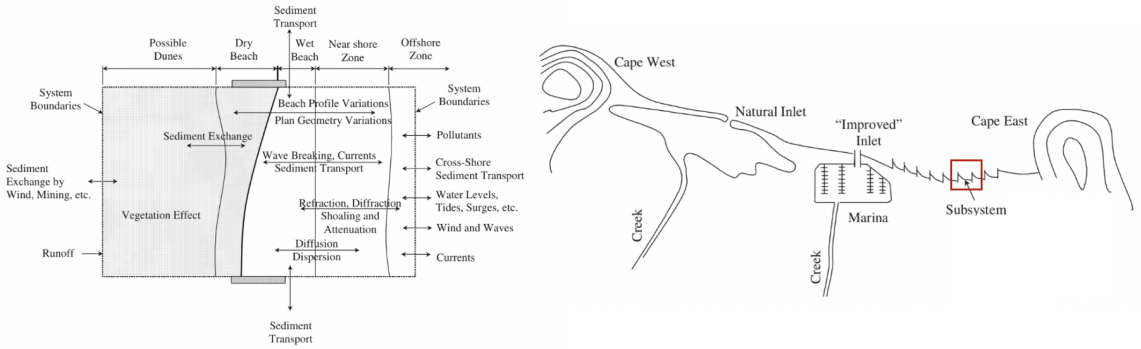


Figure 1.7: Left: Physical sub-system example showing the inputs, outputs, and boundaries relevant to sediment transport analysis. Right: Coastal system.[15]

As coastal development intensifies, so does the demand for protection, since most natural coastal ecosystems cannot offer the level of protection required by highly developed coastal societies. Coastal engineering solutions therefore span a wide spectrum. A large range of possible combinations between fully engineered hard structures (e.g. dikes, breakwaters, groins see Figure 1.8) and entirely nature-based approaches (e.g. beach-dune systems, salt-marsh protection and reconstruction, mangroves see Figure 1.9) exists. For example, dune ecosystems can offer high level flood protection by dissipating wave energy. However, sustainability on sediment-starved coasts often depends on groins, which retain sand and preserve the beach buffer necessary for dune maintenance [35].

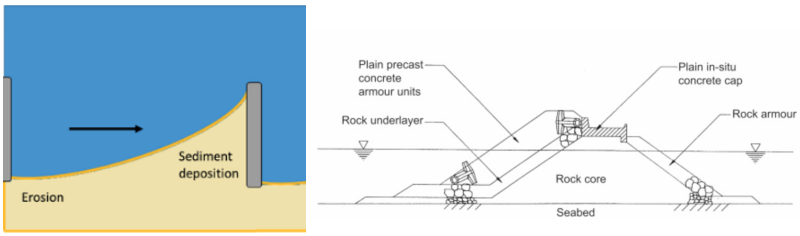


Figure 1.8: Examples of hard engineering coastal protection structures. Left: Groins [24]. Right: Rubble mound breakwater [30].

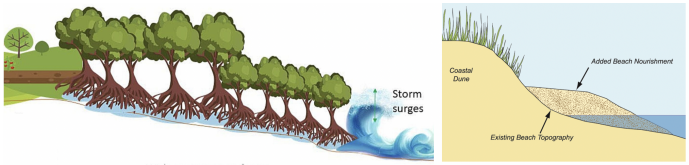


Figure 1.9: Examples of natural coastal protection. Left: Mangroves[31]. Right: Beach-dune system (Source: Northeast Regional Ocean Council).

Among hard engineering solutions, storm surge barriers represent a structurally, technically and economically viable response to coastal flood risk. They are designed to protect densely populated urban and economic areas against extreme surge events [33].

1.4 Storm Surge Barriers

A storm surge barrier is a partially movable structure built across an estuary or river branch that can be closed temporarily. Its primary function is to protect low-lying areas from flooding during storm surge events. During normal conditions, the barriers remain open. In its general configuration, such a structure comprises a gated section through which flow is regulated, a fixed dam section, and in some cases a navigation lock [25].

A storm surge barrier has several secondary purposes. It must accommodate river run-off during closure periods, maintain navigability for maritime traffic, and in some cases provide a road crossing. Water quality considerations are also significant. In semi-enclosed water bodies such as the Venice Lagoon, barrier closure restricts the exchange of seawater with the open sea, altering salinity gradients and reducing circulation. It can have pronounced ecological consequences. Their design and operation thus involve a fundamental tension between maximum flood protection and minimal disruption to the natural functioning of the coastal system [25].

It is important to distinguish storm surge barriers from two related but distinct structure types. Closure dams permanently seal off an estuary from the sea, converting the inner water body into a freshwater lake and eliminating tidal exchange entirely. Tidal barrages are designed to generate electricity from tidal energy and require a tidal range $\geq 5\,m$. The movable section of the storm surge barrier must be large enough to allow sufficient tidal and residual circulation under normal conditions [25].

Storm surge barriers generally incorporate more advanced technology than alternative flood defense structures, and consequently have relatively high capital and maintenance costs. They are therefore considered appropriate for prosperous, densely developed coastal areas where the preservation of ecological conditions, continued navigation, and urban quality of life justify the associated investment [25]. These structures have life spans in the order of 100 years [33].

Only a limited number of such structures exist worldwide, over 50 in 2023. Well known examples include the Maeslantkering barrier (1.12), the Thames barrier (1.10) and obviously, the MOSE Barrier (1.5) [33]. Existing barriers may be compared according to several characteristics: the period of construction, the total barrier length, the cumulative span of the gated section, the hydraulic gate type employed, and the geometric dimensions of sections dedicated to navigation and to flow passage. To provide an overview before examining the MOSE system in detail, the following section introduces two representative operational barriers.

Thames Barrier



Figure 1.10: Thames barrier in closed condition. Source: Environment Agency (UK)

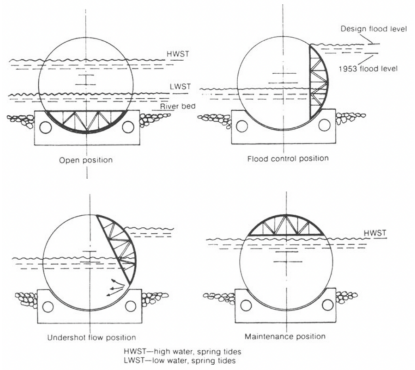


Figure 1.11: Working principle [37]

The Thames Barrier consists of rotary segment gates (Figure 1.11). It operates in a tidal range of approximately 5 m and serves both flood protection and navigation purposes, with water quality as an additional consideration. The barrier spans 520 m across the River Thames. Nine concrete piers divide the river into ten sections ranging from 30 to 61 m, each with a radial gate [25].

Maeslant Barrier

The Maeslant consists of two horizontal sector-gates stored in docks on either side of the Nieuwe Waterweg river (Figure 1.12). Each gate is 210 m wide and supported by 237 m long trusses [33]. It is one of the largest movable flood defense structures in the world. Its sole secondary function is navigation, as the waterway serves as the main access route to the port of Rotterdam [25]. The construction began in 1991 and the barrier became operational in autumn 1997.



Figure 1.12: Maeslantkering in closed condition. Source: Rijkswaterstaat, NL.

It was designed to only close, on average, once every 10 years when the water level in Rotterdam is forecast to reach 3 m above mean sea level. The barrier's closing takes approximately 3 h [33].

1.5 The MOSE System

1.5.1 Operating Principle

The MOSE system consists of 78 independent mobile flap gates, each hinged at the bottom of the inlet channel [26]. Conceived following the catastrophic 1966 flooding, the project required more than 40 years of design and construction [28], at a total cost of approximately 6 billion euros (excluding operational costs) [12]. The system has been operational since October 2020 and has already been activated over one hundred times [28]. Its operating principle is illustrated in Figure 1.13.

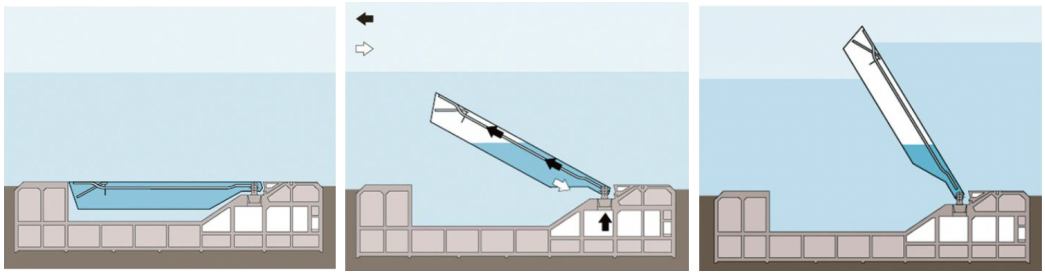


Figure 1.13: Left: MOSE gate in open (submerged) position, filled with water. Center: Gate being raised as water is evacuated and replaced with compressed air. Right: Gate in closed position. Source : Consorzio Venezia Nuova 2010 (CVN).

Normal Conditions : Under normal tidal conditions, the gates are filled with water, they lie flat in their caissons on the bed of the inlet channel. They are hidden from view and allow free navigation and water circulation.

Activation : When tidal forecasts predict water levels exceeding 110 cm above mean sea level (the safeguarding level) the barriers are activated. Compressed air is injected into the gates, expelling the water and rotating them upward about their hinges to their operational angle.

Gate in Closed Position : During closure, navigation in and out of the lagoon remains possible through dedicated locks (one lock for large vessels and three smaller for fishing boats and other small craft). On average, the barriers remain closed for approximately 4 to 5 hours (duration of the tidal event and the time required to raise and lower the gates). However, closures can extend significantly longer. This is illustrated in Figure 1.14, which shows the gate angles recorded during the storm surge of 22 November 2022. It was one of the highest tides ever registered and some inlets remained closed for up to 20 hours. The raising and lowering procedures last approximately one hour.

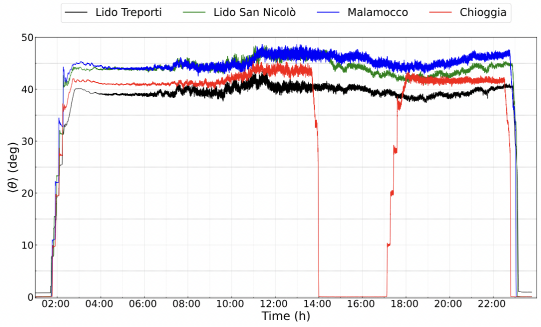


Figure 1.14: Time series of the four barriers on the November 22nd.[28]

The main geometric characteristics of each inlet and its corresponding barrier are summarized in Table 1.2.

Inlet	Channel depth [m]	Barrier length [m]	Gates number	Gate thickness [m]	Gate length [m]	Design angle [deg]
Lido Treporti	6	420	21	3.6	18.6	40
Lido San Nicolò	12	400	20	4.0	26.7	45
Malamocco	14	380	19	4.5	29.55	45
Chioggia	11	360	18	5	27.25	42.5

Table 1.2: Design characteristics of the barriers and the lagoon inlets [28]

1.5.2 Performance and Longtime Effectiveness

The MOSE system is designed to protect the lagoon from tidal levels up to 3 m above mean sea level, and is expected to remain effective for sea level rise up to 50 cm above current mean sea level (a threshold unlikely to be reached before 2080)[26]. However, as discussed in Section 1.1.1 and illustrated in Figure 1.1, projections are subject to considerable uncertainty. Under high-emission scenarios (RCP 8.5), sea level rise could reach up to 110 cm by 2100. At this level the system would no longer be sufficient. A relative sea level rise of only 30 cm would already generate almost 100 closures per year [23]. Beyond a certain threshold, the barriers would need to remain closed almost permanently, opening only during low tide.

1.5.3 Engineering and Operational Challenges

Tidal Forecasting

[34] The operation of the MOSE system relies on a complex decision protocol combining real-time water level measurements with atmospheric and oceanographic forecasting. The decision to activate the barriers is primarily driven by tidal level predictions. Forecast accuracy is a critical operational requirement [34].

Storm surge forecast quality depends on the accuracy of meteorological inputs and the resolution of basin geometry. Since the atmosphere is more chaotic than the ocean, errors in weather forecasts propagate into surge predictions and dominate forecast uncertainty over time. Several improvements have been identified to address these limitations: Refining meteorological forecasts, developing ensemble forecasting approaches, assimilating real-time water level measurements, and adopting a multi-model strategy. [34]

Increasing Closure Frequency

As the frequency of activations increases, two major concerns arise : Ecological impact and maritime traffic disruption. Each closure isolates the lagoon from the Adriatic, reducing water and sediments exchange and potentially degrading water quality over time [26].

However, several factors limit these ecological risks. High water events occur mainly in winter when biological activity is low, and even brief openings would be sufficient to flush out most pollutants. Furthermore, since the barriers consist of indepen-

dent gates, partial closures are possible. Optimal management of the system will play a key role in balancing flood protection, port activities, and lagoon ecosystem preservation [23].

1.6 Summary and Transition

The MOSE gates are subjected to complex hydrodynamic loading combining wave action, tidal forcing, and storm surge. This is giving rise to a fluid-structure interaction problem characterized by large structural rotations and a continuously evolving free surface. Accurately capturing this coupled behavior requires a numerical method capable of handling large free-surface deformations, moving boundaries, and fluid-structure interaction simultaneously. This is precisely the scope of the Particle Finite Element Method (PFEM), which is presented in the following chapter.

Chapter 2

The Particle Finite Element Method

In order to track the impact of the MOSE gate on the flow, we first consider an imposed motion, with the main focus on the Particle Finite Element Method. The method is then extended to a force-based control of the system (Chapter 4). This becomes more numerically intricate as the fluid and solid motions must be coupled. In this chapter, the method is presented in detail.

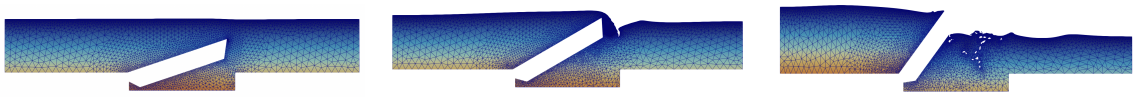


Figure 2.1: PFEM simulation: initial, during displacement, and final configurations.

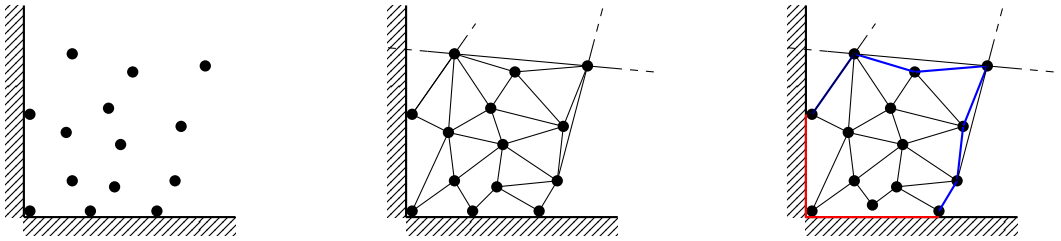
Many engineering flows involve free surfaces that evolve in complex and highly transient ways, such as in hydraulics, naval engineering, additive manufacturing, or combustion. The main numerical challenge is to represent accurately the moving free surface. Indeed, its shape and topology evolve continuously over time. Two approaches exist: interface capturing on a fixed mesh, and interface tracking, where the mesh follows the surface.

The PFEM is a mesh-based Lagrangian tracking method. The fluid domain is represented by particles that move with the flow and that carry all relevant fields (velocity, pressure, temperature, etc.) without prescribed nodal mass. An initial particle distribution is generated, typically from a mesh representing the initial geometry. The mesh is then reconstructed at each time step using Delaunay triangulation. It makes mesh quality a critical factor.

2.1 Iterative Algorithm and Procedure

Figure 2.1 is a typical example of a PFEM simulation. PFEM solves the equations of motion using a finite element formulation. In this case, the governing equations are the Navier-Stokes equations in incompressible form. Appropriate boundary conditions are applied to represent solid walls, free surfaces, inflows, and outflows, ensuring the accuracy and the stability of the simulation. PFEM is particularly suitable for strongly deforming flows and has been successfully applied to fluid–structure interactions, landslides, and solid mechanics problems [18].

The iterative numerical procedure can be divided into three main steps : the geometry detection, the resolution, and the advection[14]. In the pure fluid case, without solid *grains*, the last two steps are relatively straightforward compared to the full PFEM-DEM procedure. These steps can be broken down as follows:



Preliminary step : Point cloud that represents the fluid

1. Triangulation of the points

2. Boundaries detection with the α-shape

3. Improved mesh quality

4. Determination of the particle's velocities

5. Updated positions

Figure 2.2: Steps of the Particle Finite Element Method (PFEM) [18]

Domain and Particle Initialization

The nodes of the initial mesh serve as fluid particles. The computational domain is defined using control nodes that represent the solid boundaries.

This preliminary step precedes the main loop, represented in Figure 2.2 , which begins with the geometry detection phase.

1. Global Triangulation
Fluid particles and control nodes are triangulated together to obtain a complete discretization of the computational domain, while enforcing the solid boundary constraints.

2. Fluid Domain Identification
The α-shape algorithm is applied to distinguish fluid elements and to detect free surfaces and interfaces. The boundaries are then detected and coloured to be assigned to the proper boundary conditions.

3. Mesh Improvement
A Delaunay-based refinement procedure is used to enhance element quality and ensure compliance with a prescribed mesh size field.

Once the geometry has been established, the system is solved.
4. Field Interpolation and Resolution
Physical quantities (such as velocity) are projected onto the updated mesh to maintain consistency between time steps. The governing equations are solved over the fluid domain.

5. Advection, Particle Update
The resulting velocity field is used to update the particle positions.

2.2 Mesh Generation and Adaptivity

Due to the particle motion, the computational domain continuously undergoes geometric and topological changes. Therefore, the shape of the fluid domain must be identified and updated at each time step. To this end, the *PFEM* employs a shape detection algorithm based on the concept introduced by Edelsbrunner [11], which generalizes the notion of the convex hull.

To clarify this concept, the following definitions are introduced. The *convex hull* of a set of particles S in 2D, is defined as the intersection of all closed half-planes containing S. A generalized disc of radius α is defined as a disc of radius α if $\alpha > 0$, the complement of a disc of radius $|\alpha|$ if $\alpha < 0$, and a half-plane if $\alpha = 0$. Then, for any real α and any set S of points in the plane, the α-*hull* of S is defined as the

intersection of all closed generalized discs of radius α that contain S. The *α-shape* has the same topology as the α-hull. However, each circular arc of radius α in the α-hull of S is replaced by a straight line segment in the α-shape of S.

Note that in Edelsbrunner's original paper, the parameter α denotes the inverse of the radius, i.e. $\alpha = 1/R$. In what follows, we adopt the convention $\alpha = R$ directly, consistent with the PFEM literature.

There exists a close relationship between α-shapes and Delaunay triangulations (see Figure 2.3). Any α-shape of S is a subgraph of the Delaunay triangulation $T(S)$.

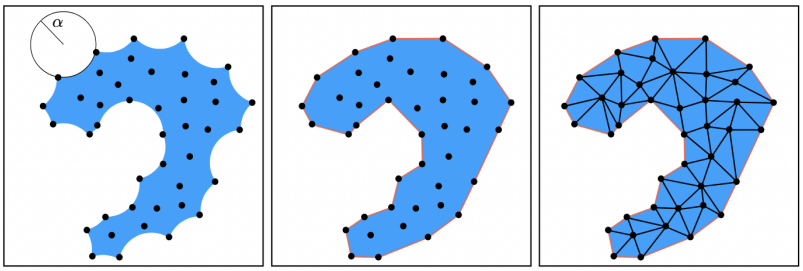


Figure 2.3: Left: α-hull of a set of points. Centre: the corresponding α-shape. Right: The Delaunay triangulation of the α-shape[18].

This provides a simple way to construct the α-shape of S. All triangles whose circumradius exceeds α are removed from $T(S)$. The boundary of the remaining domain corresponds to the α-shape of S.

In this context, α is treated as a spatially varying field, $\alpha = \alpha(\mathbf{x})$ where x denotes the position vector. Let $\mathbf{x}_e$ denote the circumcenter of element e, and R_e its circumradius. We then define the dimensionless parameter $\alpha_e = \frac{R_e}{\alpha(\mathbf{x}_e)}$. Triangles for which α_e exceeds a given threshold are removed from the fluid domain. As shown in Figure 2.4, the α-shape is thus obtained by filtering the Delaunay triangulation through a simple geometric criterion, making it well suited for tracking the evolution of the fluid domain at each time step.



Figure 2.4: Construction of the α-shape of the set of fluid particles based on the Delaunay triangulation. The green element is retained in the fluid domain (circumradius below the prescribed value), while the red element is discarded. Boundaries are naturally detected by the algorithm. [18]

To generate the initial mesh, we use a Delaunay-based mesh generator (GMSH). A mesh generator produces a triangulation that attempts to satisfy three goals. First, the union of triangles should cover the domain and respect boundary segments. Second, the triangles should be relatively well-shaped. Triangles with large or small angles can degrade the quality of the numerical solution, respectively leading to a high discretization error or a poorly conditioned FEM system. Third, the triangle size should be controllable to balance computational cost and accuracy [29].

Particles are advected as the fluid evolves. The mesh deforms accordingly. This progressive deformation leads to element degradation. Some triangles become flat or distorted and it degrades the accuracy of the numerical solution as well as the representation of the free surface.

To ensure that the element size remains controlled, mesh adaptation is performed. This work builds on the adaptive mesh refinement technique developed in [18], which was proposed for the PFEM to address this challenge using Chew's constrained Delaunay refinement. Two points need to be detailed.

The core idea of Chew's algorithm for Delaunay refinement is as follows. A triangle is considered of poor quality if it is too "flat" or too "elongated". The metric used to quantify this is the ratio of a triangle's circumradius R_e to the length of its shortest edge l. A well-shaped, nearly equilateral triangle has a small ratio, while a degenerate triangle has a large one. Any triangle whose circumradius-to-shortest edge ratio exceeds a given bound B is split by inserting a vertex at its circumcenter (see Figure 2.5). Placing the new point at the circumcenter guarantees that the Delaunay property is restored after re-triangulation, and that the poor-quality triangle

is eliminated. The process is then repeated iteratively until all triangles satisfy the quality criterion [29].

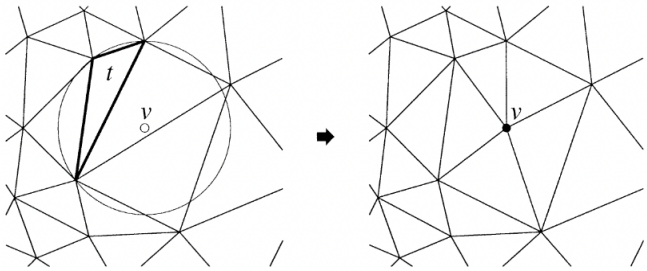


Figure 2.5: Illustration of Chew's Delaunay refinement: a poor-quality triangle is split by inserting a vertex at its circumcenter [29].

To further control the local element size, the refinement is guided by a spatially varying size field. Rather than refining uniformly over the entire domain, the mesh is kept fine in regions where an accurate geometrical or physical description is critical, and coarser elsewhere in the bulk of the fluid, where the solution varies more smoothly.

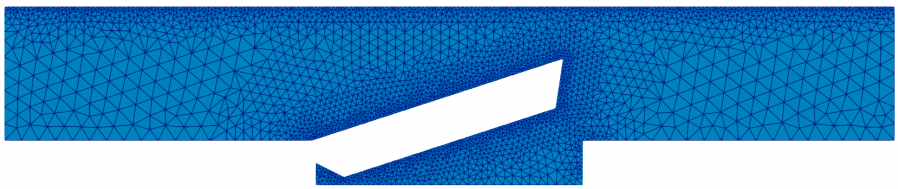


Figure 2.6: MOSE system mesh refinement

In the context of this work (see Figure 2.6), two types of regions require a fine mesh. First, the free surface, where the interface between the fluid and the surrounding air must be captured accurately. A coarse mesh there would lead to a poor representation of the fluid boundary and degrade the α-shape detection.
Second, the solid boundaries of the system, such as the contour of the MOSE barrier, where the fluid-structure interaction takes place and where accurate stress and pressure fields are needed.
This adaptive strategy allows a significant reduction in the total number of degrees of freedom compared to a uniformly fine mesh, while preserving accuracy where it matters most, striking a practical balance between computational efficiency and solution quality [14].

2.3 Governing Equations

A brief recall of material and spatial coordinates, as well as reference and current configurations is provided. Material coordinates X identify individual material points in the reference configuration, while spatial coordinates x specify their positions in the current configuration. In the Lagrangian description adopted here, the motion of the body is described by a mapping $\mathbf{x} = \boldsymbol{\phi}(\mathbf{X}, t)$, which gives the spatial position of each material point as a function of time. This contrasts with the Eulerian description, where one tracks the material point located at a given spatial position via $\mathbf{X} = \boldsymbol{\phi}^{-1}(\mathbf{x}, t)$ [4]. In this work, the governing equations are expressed using an updated Lagrangian formulation, i.e., they are written in the current configuration.

Let Ω denote the domain occupied by the fluid in the current configuration, and $\partial\Omega$ its boundary. At a given time t and in the current configuration x, the Eulerian form of the incompressible Navier–Stokes equations read:

$$\rho \frac{Du_i}{Dt} = -\frac{\partial p}{\partial x_i} + \mu \frac{\partial}{\partial x_j}\left(\frac{\partial u_i}{\partial x_j} + \frac{\partial u_j}{\partial x_i}\right) + \rho\, b_i \quad \text{in } \Omega \tag{2.1}$$

$$\frac{\partial u_i}{\partial x_i} = 0 \quad \text{in } \Omega, \tag{2.2}$$

where $\frac{D(.)}{Dt} = \frac{\partial}{\partial t} + u_j \frac{\partial}{\partial x_j}$ is the Lagrangian, or material, derivative of the quantity $(.)$. $\rho(\mathbf{x}, t)$ is the current density, μ is the dynamic viscosity, $\mathbf{u} = \mathbf{u}(\mathbf{x}, t)$ is the velocity vector, $p = p(\mathbf{x}, t)$ is the pressure, and $\rho\, \mathbf{b}(\mathbf{x}, t)$ is some body force, such as gravity [3].

Equation (2.1) expresses the conservation of linear momentum for a fluid particle. The equation relate the acceleration of the fluid particle to the pressure gradient, viscous stresses, and body forces, the continuum equivalent of Newton's second law. Equation (2.2) enforces mass conservation under the incompressibility assumption. The velocity field is required to be divergence-free.

In the Lagrangian framework adopted here with PFEM, the mesh nodes move with the fluid. The material derivative $\frac{D(\cdot)}{Dt}$ therefore reduces to the local time derivative $\partial/\partial t$. The convective term $u_j \frac{\partial u_i}{\partial x_j}$ is implicitly accounted for by the nodal displacement at each time step, as described in Section 2.4. The Lagrangian form of the NS

equations is expressed as:

$$\rho \frac{\partial u_i}{\partial t} = -\frac{\partial p}{\partial x_i} + \mu \frac{\partial}{\partial x_j} \left(\frac{\partial u_i}{\partial x_j} + \frac{\partial u_j}{\partial x_i} \right) + \rho\, b_i \quad \text{in } \Omega \tag{2.3}$$

These equations must be complemented with Dirichlet and Neumann boundary conditions:

$$\mathbf{u}(\mathbf{x}, t) = \bar{\mathbf{u}}(\mathbf{x}, t) \quad \forall \mathbf{x} \in \Gamma_D \tag{2.4}$$

$$\boldsymbol{\sigma}(\mathbf{x}, t)\, \mathbf{n} = \bar{\mathbf{t}}(\mathbf{x}, t) \quad \forall \mathbf{x} \in \Gamma_N \tag{2.5}$$

where $\bar{\mathbf{u}}(\mathbf{x}, t)$ and $\bar{\mathbf{t}}(\mathbf{x}, t)$ are the prescribed velocity and surface traction, respectively. $\boldsymbol{\sigma}(\mathbf{x}, t)$ is the Cauchy stress tensor, and $\mathbf{n}$ is the unit outward normal to the boundary. $\Gamma_D \cup \Gamma_N = \partial\Omega$ and $\Gamma_D \cap \Gamma_N = \varnothing$ [3]. A more detailed discussion of the boundary conditions will be provided later 2.5.

The Cauchy stress tensor is decomposed into an isotropic and a deviatoric part [22]:

$$\boldsymbol{\sigma} = -p\mathbf{I} + \boldsymbol{\tau} \tag{2.6}$$

with p the pressure, $\mathbf{I}$ the unit tensor and where $\boldsymbol{\tau}$ is the deviatoric (viscous) stress tensor. For a Newtonian fluid, it is related to the rate of strain tensor as:

$$\boldsymbol{\tau} = 2\mu\boldsymbol{\epsilon} \tag{2.7}$$

where the strain rate tensor is defined by [9]:

$$\boldsymbol{\epsilon} = \frac{1}{2} \left(\nabla \mathbf{u} + (\nabla \mathbf{u})^T \right) \tag{2.8}$$

Using the constitutive relation for a Newtonian fluid, the viscous term in Eq. (2.1) can be expressed in terms of the divergence of the stress tensor.

To solve these equations, the Finite Element Method is employed. The velocity and pressure fields are approximated using equal-order linear interpolation (P1/P1) over the discretized domain [14]. The resulting stability issues are addressed in Section 2.6. To remedy this, stabilization terms are added to the weak form of the governing equations.

2.4 Advection

After the geometry determination and the resolution, the final step of the algorithm consists in moving particles and grains based on their respective velocities. A second-order scheme is used for the fluid phase.

$$\mathbf{x}^{n+1} = \mathbf{x}^n + \mathbf{u}^{n+1}\Delta t + \frac{1}{2}\frac{\mathbf{u}^{n+1} - \mathbf{u}^n}{\Delta t}\Delta t^2, \tag{2.9}$$

where $\mathbf{x}$ are the nodal positions of the fluid and $\mathbf{u}$ the nodal velocities [14]. This approach ensures a consistent advection of the nodes while accounting for local acceleration, improving numerical stability and accuracy (compared to a simple first-order Euler update).

2.5 Boundary Conditions

As mentioned in Section 2.3, the Navier-Stokes equations must be complemented with appropriate boundary conditions to ensure numerical stability and physical fidelity. In this section, the boundary conditions relevant to the present work are presented, covering wall boundaries, the free surface, and cavity interfaces. While a wide variety of boundary conditions exist in the literature, only those pertaining to the modelling of the MOSE system are discussed here.

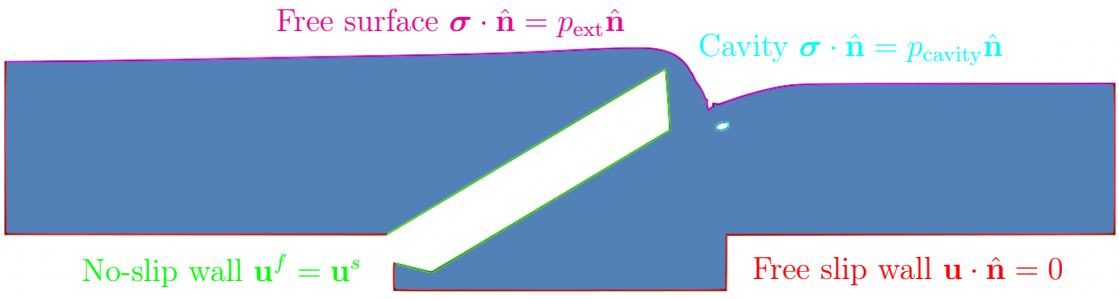


Figure 2.7: Boundary conditions along the fluid in the first configuration

2.5.1 Solid Wall Boundary Conditions

At the interface between a fluid and a solid, two boundary conditions are commonly used: the free-slip and the no-slip condition. The free-slip condition, usually employed for inviscid flows, prescribes equality of the normal velocity components at

the interface,

$$\mathbf{u}^f \cdot \hat{\mathbf{n}} = \mathbf{u}^s \cdot \hat{\mathbf{n}}, \tag{2.10}$$

allowing the fluid to slide tangentially along the solid surface.

The no-slip condition, appropriate for viscous flows, enforces full velocity continuity at the interface,

$$\mathbf{u}^f = \mathbf{u}^s, \tag{2.11}$$

meaning the fluid adheres to the solid and cannot slide.

The choice between these two conditions is closely related to the Reynolds number and the resulting boundary layer structure. The Reynolds number $Re = \frac{\rho U L}{\mu}$ characterizes the ratio of inertial to viscous forces, with U and L denoting characteristic velocity and length scales of the problem. At high Reynolds number, viscous effects are confined to a thin region near the wall, the boundary layer. Its thickness δ can be orders of magnitude smaller than the characteristic problem size. Resolving this layer would require an extremely fine near-wall discretization, which is often computationally prohibitive.

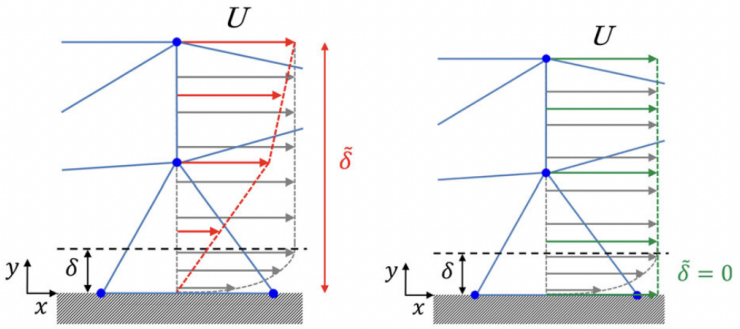


Figure 2.8: Velocity profile approximation near a solid wall on a coarse mesh: no-slip condition (left) versus free-slip condition (right). When δ is much smaller than the element size, the free-slip condition better captures the bulk flow kinematics [3].

As illustrated in Figure 2.8, on a coarse mesh, a no-slip condition artificially increases the boundary layer thickness δ to the size of the near-wall element, introducing a larger error than a free-slip condition. However, free-slip conditions do not account for the dissipation introduced at the fluid–solid boundary [3].

In the present work, a free-slip condition is applied on all fixed walls (shown in red

in Figure 2.7), meaning that only the normal velocity component is constrained,

$$\mathbf{u} \cdot \hat{\mathbf{n}} = 0 \tag{2.12}$$

while the fluid is free to slide tangentially along the surface. Given the scale of the system and the high Reynolds number regime, resolving the boundary layer at the fixed walls would require a prohibitively fine near-wall discretization without meaningful gain in accuracy for the quantities of interest. The free-slip condition is therefore the appropriate choice on an under-resolved mesh, as discussed above.

On the mobile barrier (shown in green in Figure 2.7), a no-slip condition is imposed instead. The fluid velocity at the interface is fully prescribed according to the rotational motion of the structure, $\mathbf{u}^f = \mathbf{u}^s$, where $\mathbf{u}^s$ is the local velocity of the barrier. This condition is motivated by the kinematic consistency of the FSI coupling. Without it, the model would neglect the tangential momentum transfer that contributes to the net torque on the structure. At high Reynolds number, this contribution is expected to remain small, it could be the subject of a sensitivity analysis.

2.5.2 Inlet/Outlet Boundary Condition

At the inlet boundary, a Dirichlet condition is imposed on the velocity field. Several profiles can be considered, ranging from a simple uniform velocity profile to a depth-dependent oscillating profile based on linear wave (Airy) theory. At the outlet boundary, two classical approaches are commonly used: imposing a zero pressure condition ($p = 0$), which allows the fluid to exit freely, or introducing a sponge layer that progressively damps the flow near the boundary to avoid spurious wave reflections.

2.5.3 Free Surface Boundary Conditions

On free surfaces, the normal fluid stress is set equal to the external atmospheric pressure,

$$\boldsymbol{\sigma} \cdot \hat{\mathbf{n}} = p_{\text{ext}} \hat{\mathbf{n}}, \tag{2.13}$$

where $p_{\text{ext}} = 0$ is taken as the reference pressure. This Neumann condition allows the interface to evolve freely under internal forces and gravity. In the present work, it is applied along the free surface of the basin (shown in pink in Figure 2.7).

2.5.4 Bubble Boundary Conditions

For cavities (bubbles) within the fluid (e.g., in light blue in Figure 2.7), an internal pressure, p_{cavity}, is applied to emulate the presence of an incompressible fluid inside these volumes,

$$\boldsymbol{\sigma} \cdot \hat{\mathbf{n}} = p_{\text{cavity}} \hat{\mathbf{n}} \tag{2.14}$$

In high-inertia simulations, the fluid can trap cavities that form bubbles. If neglected, these bubbles are treated as voids and eventually disappear, violating local mass conservation. When the internal bubble dynamics are much faster than the surrounding fluid, as is typical for high fluid-to-bubble density ratios (e.g., water-air), the bubble can be modelled as an incompressible region without explicitly simulating its flow. A boundary condition is applied at the bubble interface to account for incompressibility, buoyancy, and surface stresses, ensuring mass conservation within each bubble while maintaining the correct fluid dynamics [18].

2.6 Stability : LBB Condition and PSPG

Since the PFEM relies on continuous remeshing procedures based on a cloud of nodes, the spatial discretization is generally restricted to linear triangular elements [17]. The remeshing strategy preserves the nodes of the previous mesh, thereby avoiding interpolation of nodal variables between successive meshes.

However, this approach limits the formulation to first-order finite elements because it complicates the use of higher-order interpolations. Indeed, higher-order elements would require the transfer of additional degrees of freedom associated with edge or internal nodes, which is not compatible with the PFEM remeshing procedure. Furthermore, the geometric curvature associated with higher-order elements would be lost at each Delaunay triangulation step [7].

As a consequence, PFEM formulations for incompressible flows commonly employ equal-order linear finite elements (P1/P1), corresponding to first-order continuous interpolation for both velocity and pressure [32]. However, the incompressible Navier–Stokes equations impose a compatibility condition between the velocity and pressure approximation spaces, known as the Ladyzhenskaya–Babuška–Brezzi (LBB) condition. This condition is necessary to ensure the stability and uniqueness of the numerical solution [17].

When equal-order interpolations are used for both velocity and pressure, the LBB condition is not satisfied [17, 6]. As a result, spurious oscillations may appear, mainly in the pressure field [32]. This constitutes the first main source of instability in incompressible finite element formulations.

A second source of instability is associated with advection-dominated flows. In classical Eulerian formulations, the convective term may lead to a loss of stability. In standard finite element formulations, this issue is commonly addressed using the Streamline-Upwind/Petrov–Galerkin (SUPG) stabilization technique, which introduces an artificial diffusion along the streamline direction while preserving the consistency of the formulation. In the present work, the PFEM formulation is fully Lagrangian. Therefore, the advection term is naturally accounted for through the motion of the mesh nodes and does not explicitly appear in the governing equations. As a result, SUPG stabilization is not required in the current approach.

To overcome the instability related to the violation of the LBB condition, Hughes and Tezduyar proposed the PSPG (Pressure-Stabilizing/Petrov-Galerkin) formulation. The PSPG stabilization allows the use of equal-order interpolation spaces for velocity and pressure while preventing spurious pressure oscillations.
The PSPG stabilization is obtained by minimizing the sum of the squared residual of the momentum equation integrated over each element domain. This procedure introduces a least-squares contribution, involving the pressure gradient and viscous stress terms. These additional terms are then added to the standard Galerkin weak formulation with an appropriate weighting parameter [32].

The effect of PSPG stabilization may also be interpreted from a spectral perspective. The PSPG formulation preserves the low-frequency pressure modes associated with the physical solution while damping the non-physical high-frequency oscillations generated by equal-order interpolation.

Finally, it should be emphasized that SUPG and PSPG stabilization terms are directly related to the mixed finite element formulation of the problem. In the present formulation, the unknown vector contains both velocity and pressure variables, which explains the necessity of introducing stabilization terms associated with the coupled velocity–pressure system.

Chapter 3

From Passive to Active Regime by Imposed Angular Velocity

This chapter uses PFEM to study the MOSE gate deployment under an imposed angular velocity. This represents a first step before the gate motion is coupled to the fluid in the next chapter. The problem setup is presented first (shared with the second simulation, in Chapter 4), followed by the simulation and its results.

3.1 Problem Description & Simplifying Assumptions

Reference Geometry

The reference geometry is illustrated in Figure 3.1. The basin of dimensions $L_{\text{basin}} \times h_{\text{basin}}$ contains a bottom-hinged gate of dimensions $L_{\text{mose}} \times t_{\text{mose}}$, articulated at C_r. As recalled from Chapter 1, the MOSE gate normally rests flat on the seabed, filled with water ($\theta = 0$, dashed red). Upon activation, compressed air displaces the water, generating a buoyant torque about C_r that drives the gate to its operational position (solid red). In the present simulations, the gate is initialised at $\theta_0 > 0$ to avoid near-flat configuration issues inherent to the PFEM framework, while preserving the essential deployment dynamics.

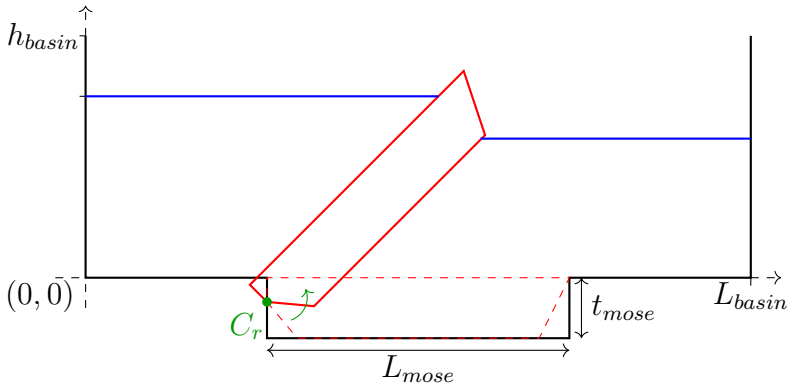


Figure 3.1: Reference geometry for the bottom-hinged gate simulations. Dashed red: gate at rest (water-filled). Solid red: gate at full deployment (air-filled). C_r: hinge point.

Simplifying assumptions

- **Incompressible fluid:** The water is modelled as an incompressible Newtonian fluid.
- **Rigid body:** The flap is treated as a rigid body rotating about a fixed hinge at its base.
- **2D planar model:** The flap gate is modelled as a two-dimensional cross-section perpendicular to the rotation axis. This reduction is justified by the large width-to-height ratio of the structure, under which spanwise end effects are negligible and the in-plane flow dominates.

Common Simulation Parameters

All simulations share the same computational domain, some of the boundary conditions, and base physical parameters, summarized in Tables 3.2 and 3.1. Simulation-specific parameters are introduced in the corresponding sections.

Boundary	**Condition**
Bottom wall	Free slip $\mathbf{u} \cdot \hat{\mathbf{n}} = 0$
Gate surface	no-slip $\mathbf{u}^f = \mathbf{u}^s$
Free surface	$\boldsymbol{\sigma} \cdot \hat{\mathbf{n}} = p_{\text{ext}} \hat{\mathbf{n}}$
Bubble	$\boldsymbol{\sigma} \cdot \hat{\mathbf{n}} = p_{\text{cavity}} \hat{\mathbf{n}}$

Table 3.1: Common boundary conditions.

Parameter	Symbol	Value	Unit
Fluid			
Fluid Density	ρ_f	1000	$\mathrm{kg/m^3}$
Bubble density	ρ_{bubble}	10^{-3}	$\mathrm{kg/m^3}$
Dynamic viscosity	μ	10^{-3}	Pa·s
Surface tension	σ	0.072	N/m
Gravitational acc.	g	9.81	$\mathrm{m/s^2}$
Geometry			
Basin width	L_{basin}	100	m
Basin height	h_{basin}	50	m
Gate length	L_{mose}	40	m
Gate thickness	t_{mose}	7.76	m
Initial fluid height	h_{fluid}	22	m
PFEM-specific			
Alpha-shape parameter	α	1.3	—
Max. element size	$s_{\max}$	2	m
Min. element size	$s_{\min}$	0.25	m

Table 3.2: Common physical and numerical parameters.

3.2 Simulation 1 — Prescribed Angular Velocity

3.2.1 Problem Setup

Objective

The objective of this first simulation is to impose a prescribed angular velocity on the barrier (see Figure 3.3) and to analyze the resulting hydrodynamic loads acting on the structure. This approach provides a controlled framework to estimate the order of magnitude and temporal evolution of the fluid-induced torque and pressure distribution. Although the motion is artificially imposed and does not result from a true fluid–structure interaction, these preliminary results are essential to calibrate subsequent simulations. In particular, they provide a physically realistic order of magnitude for a potential motor torque. This leads to a more accurate and predictive representation of the coupled system dynamics.

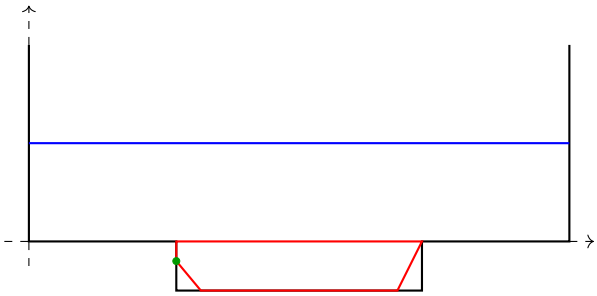


Figure 3.2: Initial Configuration

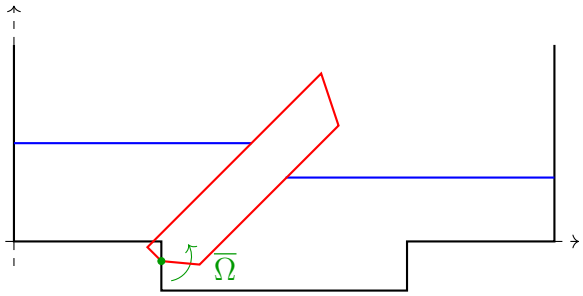


Figure 3.3: Rotated Configuration

Prescribed Angular Velocity Profiles

Two distinct angular velocity profiles are investigated in this simulation.

Profile 1 — Step function. The simplest prescription consists of a constant angular velocity $\omega_{\max}$ applied over the entire range of motion, with an abrupt cutoff once the barrier reaches its operational angle θ_f:

$$\omega_1(t) = \begin{cases} \omega_{\max} & \text{if } \theta_1(t) < \theta_f, \\ 0 & \text{if } \theta_1(t) \geq \theta_f. \end{cases} \tag{3.1}$$

Profile 2 — Smooth Gaussian profile. In order to obtain a smoother and more realistic motion, we implement a progressive profile based on the Gaussian probability density function. The angular velocity gradually increases from zero in $t = 0$ to $\omega_{\max}$ at the mid-manoeuvre time $t_m = t_{end}/2$ and then symmetrically decreases back to zero in t_{end}. The angular displacement is modelled as the cumulative distribution function (CDF) of a normal distribution centred at t_m:

$$\theta_2(t) = \theta_0 + \frac{\theta_f - \theta_0}{2} \left[1 + \operatorname{erf}\left(\frac{t - t_m}{\sigma\sqrt{2}} \right) \right], \tag{3.2}$$

where erf denotes the Gauss error function. Differentiating (3.2) with respect to time yields the prescribed angular velocity:

$$\omega_2(t) = \frac{\theta_f - \theta_0}{\sigma\sqrt{2\pi}} \exp\left(-\frac{(t - t_m)^2}{2\sigma^2} \right). \tag{3.3}$$

$$\sigma = \frac{\theta_f - \theta_0}{\omega_{\max}\sqrt{2\pi}}. \tag{3.4}$$

with σ the shape parameter.

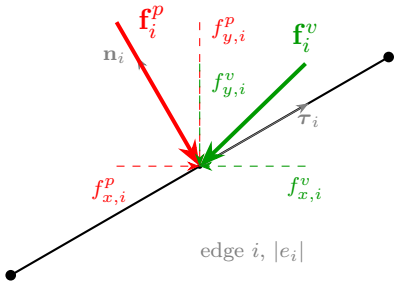
Simulation Parameters

The simulation-specific parameters are summarised in Table 3.3.

Parameter	Symbol	Value	Unit
Initial angle	θ_0	$\pi/10$	rad
Final angle	θ_f	$\pi/4$	rad
Maximum angular velocity	$\omega_{\max}$	$2\pi/100$	rad/s
Manoeuvre duration	t_end	20	s
Symmetry instant	t_m	10	s
Maximum velocity	$v_{\max}$	$2\omega L_{mose}$	m/s
Time step	Δt	$0.1\frac{s_{min}}{v_{max}}$	s

Boundary	Condition
Vertical walls	Free slip $\mathbf{u}\cdot\hat{\mathbf{n}} = 0$
Bubble	no bubble

Table 3.3: Simulation 1 parameters and common boundary conditions (all other parameters as in Table 3.2).



Variable	Size	Definition
`f_all`	$(n_e, 4)$	Components $[f_{x,i}^p,\ f_{y,i}^p,\ f_{x,i}^v,\ f_{y,i}^v]$
`local_forces_p`	$(n_e, 2)$	Pressure force $\mathbf{f}_i^p = -p_i\,\mathbf{n}_i\,\lvert e_i\rvert$
`local_forces_v`	$(n_e, 2)$	Viscous force $\mathbf{f}_i^v = (\boldsymbol{\tau}\cdot\mathbf{n}_i)\,\lvert e_i\rvert$
`forces_edge`	$(n_e, 2)$	Total force per edge $\mathbf{f}_i = \mathbf{f}_i^p + \mathbf{f}_i^v$

Figure 3.4: Force decomposition on the MOSE boundary edges. $\mathbf{f}_i^p$: pressure force (normal to edge). $\mathbf{f}_i^v$: viscous force. $\mathbf{n}_i$: outward unit normal. $|e_i|$: edge length.

3.2.2 Results

Curvilinear Abscissa s

To represent the distribution of hydrodynamic forces along the MOSE boundary, a curvilinear abscissa s is introduced. Since the boundary edges are unordered, the function `get_curvilinear_coordinates` is implemented and proceeds in two steps.

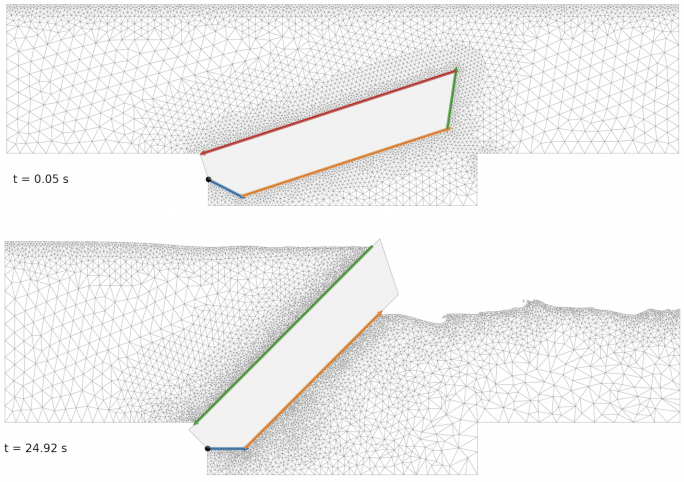


Figure 3.5: Face partition of the MOSE boundary at $t = 0.05$ s and $t = 24.92$ s. Each color identifies a distinct face, as detected by the `get_curvilinear_coordinates` function.

1) Boundary edges are grouped into faces by clustering their outward unit normals. Edges that share approximately the same normal direction (within a 10° tolerance) are assigned to the same face. This yields the face partition visible in Figure 3.5, where each color corresponds to a distinct face.

2) Within each face, the edges are ordered by projecting their midpoints onto the face direction, starting from the endpoint closest to the center of rotation. The local arc length is then accumulated across faces, producing a global parameter $s \in [0, s_{tot}]$, where s_{tot} corresponds to the total wetted perimeter. Only faces in contact with the fluid contribute to s, so the parameter ranges from 0 to 3 face-lengths depending on the instantaneous submersion state.

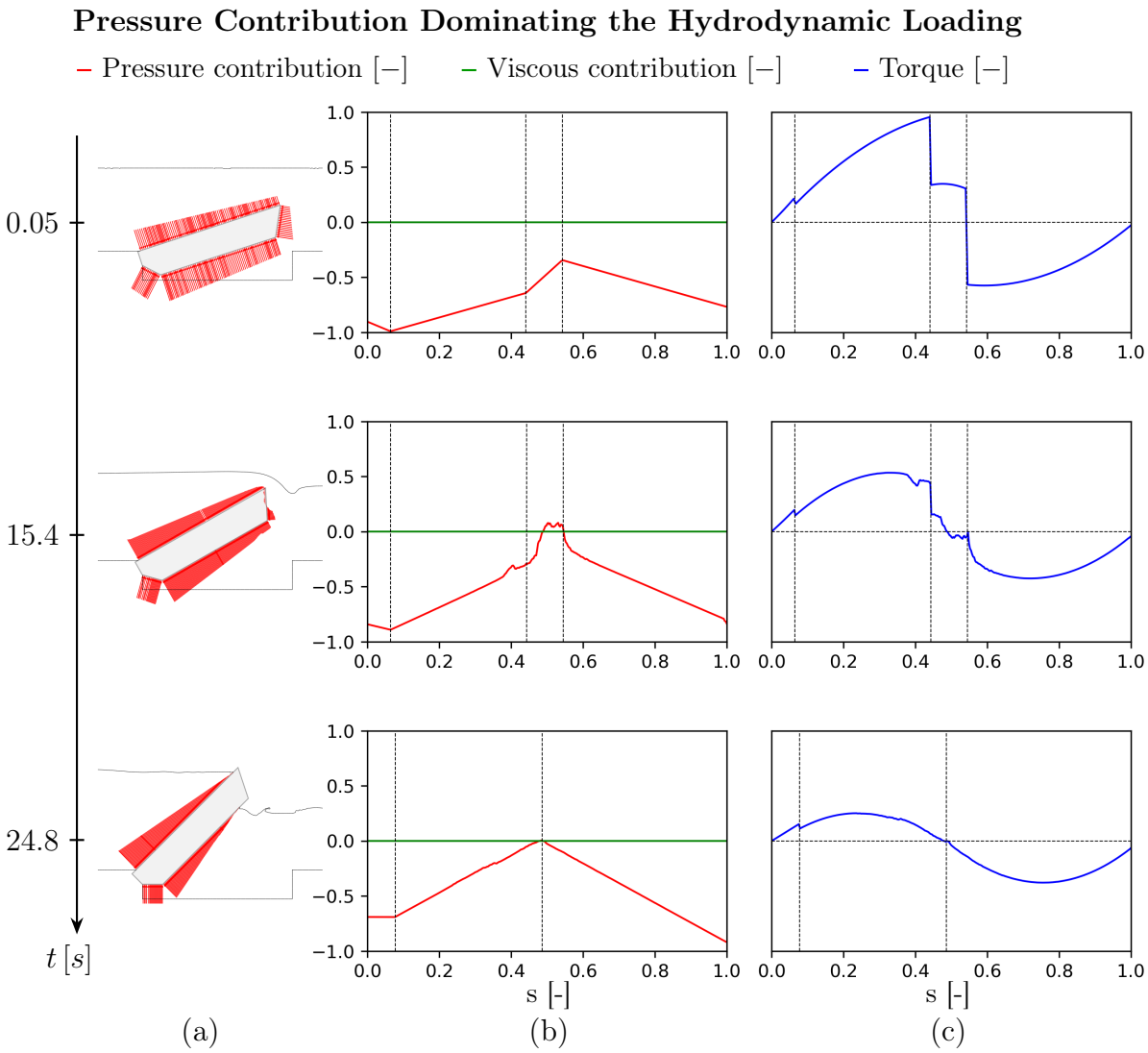


Figure 3.6: Snapshots at $t = 0.05$ s, $t = 15.4$ s and $t = 24.8$ s. (a) Pressure force distribution along the MOSE boundary. (b) Normal pressure and viscous force densities as a function of the curvilinear abscissa. (c) Torque density as a function of the curvilinear abscissa.

Figure 3.6(b) shows that the viscous contribution is negligible compared with the pressure contribution. As an example, at $t = 15.4\,\text{s}$, $\|\mathbf{F}_p\| = 1.1 \times 10^6\,\text{N}$ and $\|\mathbf{F}_v\| = 7.2 \times 10^{-2}\,\text{N}$. This behavior is consistent with the large characteristic dimensions of the problem and the associated high Reynolds number. The Reynolds number indicates that viscous effects are weak compared with inertial effects. As a result, the flow dynamics are primarily governed by inertia and pressure forces.

$$U \simeq \omega L_{\text{mose}}, \qquad Re = \frac{\rho U L}{\mu} \simeq \frac{\rho \omega L_{\text{mose}}^2}{\mu} \simeq 10^7 \tag{3.5}$$

Figure 3.6(a) and (b) show that the pressure distribution is dominated by hydrostatic effects. Since the gate remains deeply submerged, the pressure increases almost linearly with depth according to the hydrostatic relation:

$$p = p_0 + \rho g h \tag{3.6}$$

with h the local water depth. The largest pressures are therefore observed near the lower part of the structure, where the water column above the gate is maximal.

As the gate rotates, the pressure distribution progressively departs from a purely hydrostatic profile. In particular, pressure variations develop near the free surface and around the moving structure, indicating an increasing influence of fluid motion on the loading distribution.

At $t = 15.4\,s$, near the free surface, low-pressure regions can be observed on the upper side of the gate. This behaviour is likely related to flow redistribution around the moving structure and to the reduced confinement of the surrounding water close to the free surface. In these regions, the fluid can move more freely, leading to a local pressure decrease. Simultaneously, pressure accumulation occurs on the lower face of the gate due to the displacement of large water masses.

At later stages of the deployment, the wetted surface decreases significantly as the gate emerges from the water. Consequently, the global hydrodynamic loading decreases (see Figure 3.6(b) and (c)).The simulation therefore captures the progressive evolution of the hydrodynamic loading during the deployment, from an initially hydrostatic-dominated pressure distribution to a reduced loading as the gate emerges from the water.

Vorticity and Zoom on the Viscous Contribution

Beyond the global force balance dominated by pressure, the flow exhibits local phenomena worth analyzing in detail. In particular, we investigate the possible onset of flow separation and recirculation.

Recirculation regions are zones where the fluid detaches from the main flow and forms closed streamline loops ($\psi = \text{const}$). They arise from the dominance of convective

inertia over viscous diffusion, from the nonlinear term $(\mathbf{u}\cdot\nabla)\mathbf{u}$ in the Navier–Stokes equations. Recirculation zones can be identified through the streamfunction Ψ , governed by:

$$\nabla^2\Psi = -\omega \tag{3.7}$$

Where the vorticity ω measures the local tendency of the fluid to rotate around itself [16]. Positive vorticity (typically represented in red) corresponds to counterclockwise rotation, whereas negative vorticity (blue) corresponds to clockwise rotation.

$$\omega = \frac{\partial v}{\partial x} - \frac{\partial u}{\partial y}, \qquad u = \frac{\partial \Psi}{\partial y}, \quad v = -\frac{\partial \Psi}{\partial x} \tag{3.8}$$

Since recirculation necessarily coincides with concentrated vorticity, monitoring ω provides a convenient indicator of flow separation, without requiring explicit streamline integration.

Although the global viscous contribution to the force balance remains weak, viscous effects still generate vorticity locally through velocity gradients near solid boundaries. In the present high-Reynolds-number configuration, flow separation and recirculation are primarily driven by inertial effects associated with the gate motion and the resulting flow acceleration. Nevertheless, these flow structures remain closely associated with concentrated vorticity regions, making the vorticity field a useful indicator of separation phenomena.

Figure 3.7(b) shows the viscous force density along the curvilinear coordinate (s). This force is directly related to tangential shear stresses generated by velocity gradients near the gate surface. The largest viscous peaks are mainly observed near the extremities of the structure, where the tangential velocity is maximal due to the rotational motion. Localized viscous peaks also coincide with regions of concentrated vorticity and flow separation. Moreover, changes in the sign of the viscous force density are associated with changes in the rotation direction of the vortical structures.

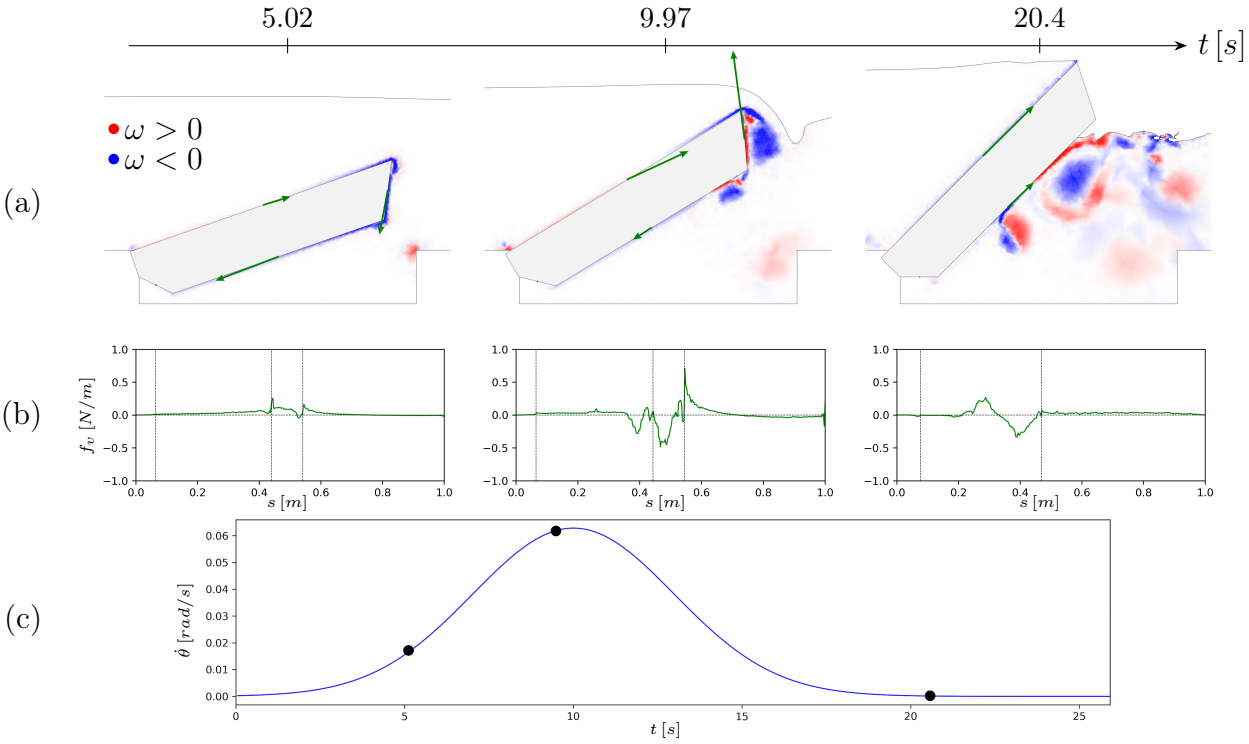


Figure 3.7: Snapshots of the barrier at different times for the Gaussian angular velocity profile. (a) Viscous force resultant per face and vorticity field. (b) Viscous force density as a function of the curvilinear abscissa. (c) Imposed angular velocity profile with markers indicating the snapshot instants.

At $t = 5.02\,s$, the angular velocity remains relatively low (Figure 3.7(c)). Consequently, both the vorticity field and the viscous force density remain weak, except for small localized peaks near sharp corners associated with geometric singularities. The boundary layer remains mostly attached to the structure.

$t = 9.97\,s$ corresponds to the almost maximum angular velocity and the end of the acceleration phase. Strong and concentrated vortical structures appear near the upper tip of the gate close to the free surface. A pair of opposite-sign vortices can be identified. This could indicate local boundary-layer detachment and flow separation induced by inertial effects. At this stage, the tangential velocity along the structure reaches its maximum value, leading to pronounced viscous peaks. The alternating positive and negative viscous stresses are consistent with the opposite rotation directions of the vortices.

At $t = 20.4\,s$, the gate motion is nearly at stop. However, the surrounding fluid still retains part of its momentum. As a result, larger recirculation structures are observed

away from the structure, together with detached vortices and a more diffuse wake. Simultaneously, the viscous force density decreases as the gate velocity becomes smaller.

It should nevertheless be noted that these viscous phenomena remain highly localized and do not significantly affect the global force balance. In addition, the present mesh resolution may artificially thicken the boundary layer, introducing some uncertainty in the estimation of viscous stresses and viscous forces.

Temporal Variation of the Resulting Forces and Torques

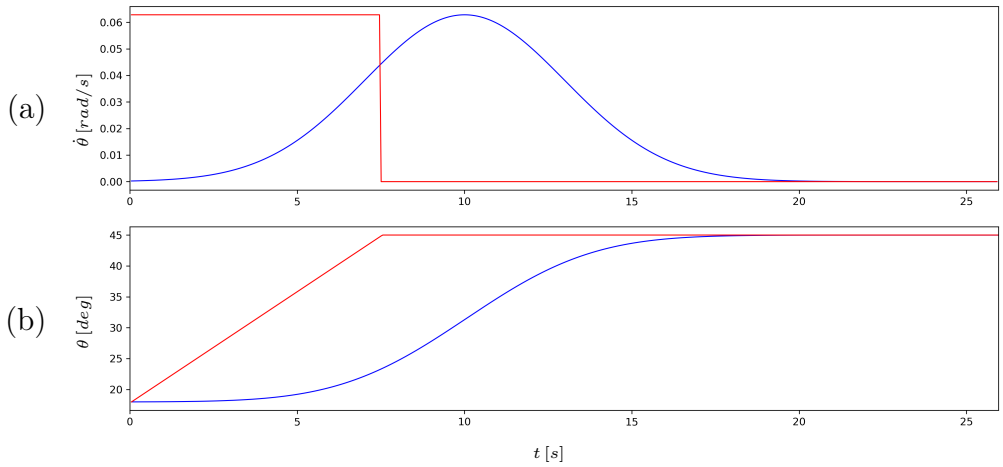


Figure 3.8: (a) Imposed angular velocity profiles: progressive (blue) and step (red). (b) Corresponding angular position θ as a function of time for both profiles.

Figure 3.9(a) presents the evolution of the resulting torque for both angular velocity profiles. For the progressive (Gaussian-like) velocity profile, the initial angular velocity remains small, leading to a smoother and more gradual torque evolution. In contrast, the step profile produces a rapid initial acceleration, generating a transient adjustment phase visible through the sharp torque variation at the beginning of the motion. A second torque peak is also observed when the gate abruptly stops, due to the sudden deceleration of the surrounding fluid.

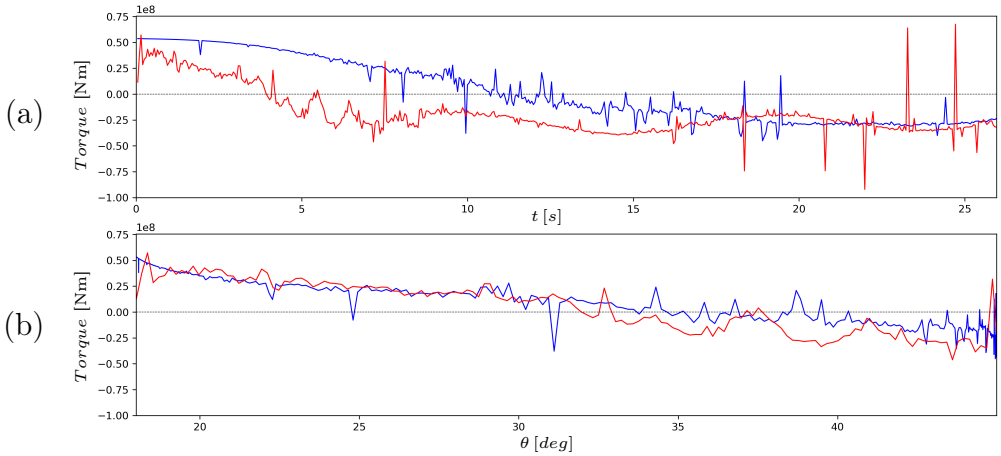


Figure 3.9: (a) Resulting torque as a function of time for both velocity profiles (blue: progressive, red: step). (b) Resulting torque as a function of the angular position θ of the barrier.

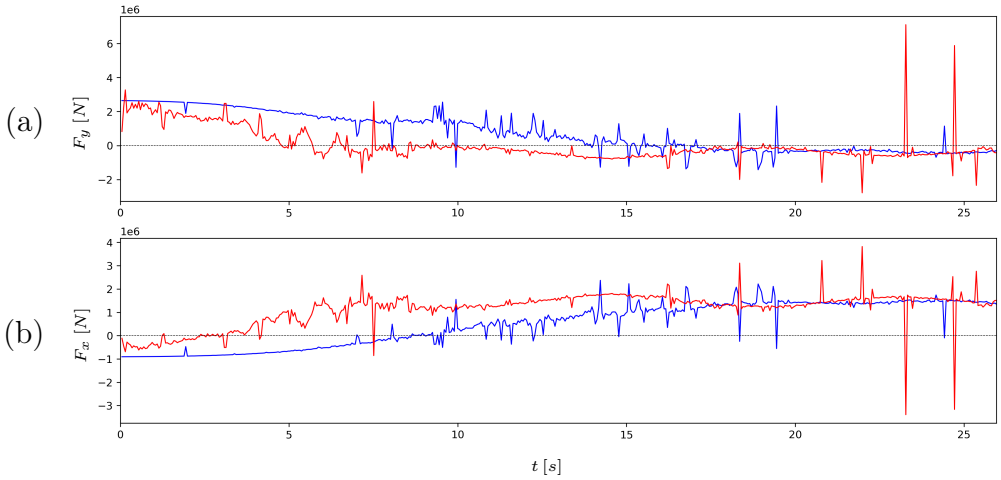


Figure 3.10: (a) y-component of the resulting forces as a function of time for both velocity profiles (same color code). (b) x-component of the resulting forces as a function of time for both velocity profiles (same color code).

For both velocity profiles, the resulting torque globally decreases during the deployment as the gate progressively emerges from the water and the wetted surface decreases. The hydrodynamic loading therefore becomes weaker at larger angular positions. Small oscillations are observed once the gate motion slows down or stops. These oscillations are associated with the residual motion of the surrounding water and the resulting fluid-structure interactions. They are more visible for the step

profile since the gate reaches its final position earlier, leaving more time for the fluid oscillations to develop.

Figure 3.9(b) shows that the torque evolution as a function of the angular position remains globally similar for both velocity profiles. This suggests that the hydrodynamic torque is primarily governed by the instantaneous immersed geometry and the displaced water volume, whereas the precise time evolution of the angular velocity mainly affects transient effects and fluctuations.

Chapter 4

A Torque Coupling

In the previous chapter, the gate motion was prescribed. Here, the gate is driven by a torque balance. Its motion results from the combination of the applied torque, the fluid loads, and inertia. Consequently, the fluid and the solid must be solved together. This is a fluid–structure interaction (FSI) problem. This chapter provides a review of FSI before applying a partitioned, PFEM-based coupling to the gate.

4.1 Fluid-Structure Interaction Review

In recent decades, the need to understand and model increasingly complex phenomena has led to the development of multiphysics coupled models (interaction between solid and fluid domains), which in most cases require numerical solutions [4]. Fluid-structure interaction (FSI) problems describe the mutual interaction between fluids and solid structures. They are of great interest both in academic research and in industrial engineering [19]. This phenomenon is encountered in various engineering fields such as heat exchangers, water loading on dike or blood flow through arteries.

Two main numerical approaches can be distinguished : monolithic or partitioned methods (see Figure 4.1).

4.1.1 Monolithic vs Partitioned Approaches

In the monolithic approach, the fluid and the solid equations are first discretized in space and time with a method of choice. This results in a system of coupled discrete

equations with the fluid and solid variables as unknowns.

$$\begin{cases} f(v,u) = 0, \\ s(v,u) = 0. \end{cases} \tag{4.1}$$

where f represents the discrete fluid flow equations, s the discrete structural equations, the vector v groups the flow variables (velocity, pressure, etc.) over the entire fluid domain, and the vector u groups the structural variables (displacement, stress, etc.) over the entire solid domain. The complete nonlinear system of fluid flow and solid displacement equations is solved simultaneously, generally using a Newton–Raphson method [9]. In each Newton–Raphson iteration, the following linear system must be solved :

$$\begin{bmatrix} \partial_v f & \partial_u f \\ \partial_v s & \partial_u s \end{bmatrix} \begin{bmatrix} \Delta v^k \\ \Delta u^k \end{bmatrix} = - \begin{bmatrix} f(v^k, u^k) \\ s(v^k, u^k) \end{bmatrix}. \tag{4.2}$$

Here, k denotes the Newton–Raphson iteration index, $\Delta v^k = v^{k+1} - v^k$, and the notation $\partial_v f$ refers to the Jacobian matrix containing the partial derivatives of $f(v,u)$ with respect to v. All blocks in the Jacobian are evaluated at (v^k, u^k) [9]. These cross-coupling terms are often difficult to derive and implement. One of the main advantages of partitioned methods over monolithic methods is that these terms do not need to be computed explicitly.

The fully coupled monolithic approach is highly robust and stable for strong fluid–structure interactions (e.g., phase transformations or viscoplastic deformation). However, it is less modular and requires more implementation efforts compared to the partitioned approach [13].

The partitioned method, on the other hand, treats each physical model separately. It allows them to be solved independently in time. This is advantageous because each physics can be highly complex on its own, and efficient, well-established solvers already exist. Partitioned schemes take advantage of these solvers by coupling them as "black boxes" that exchange only the necessary information such as forces, displacements, velocities, or pressures at the fluid–structure interface [13] [4].

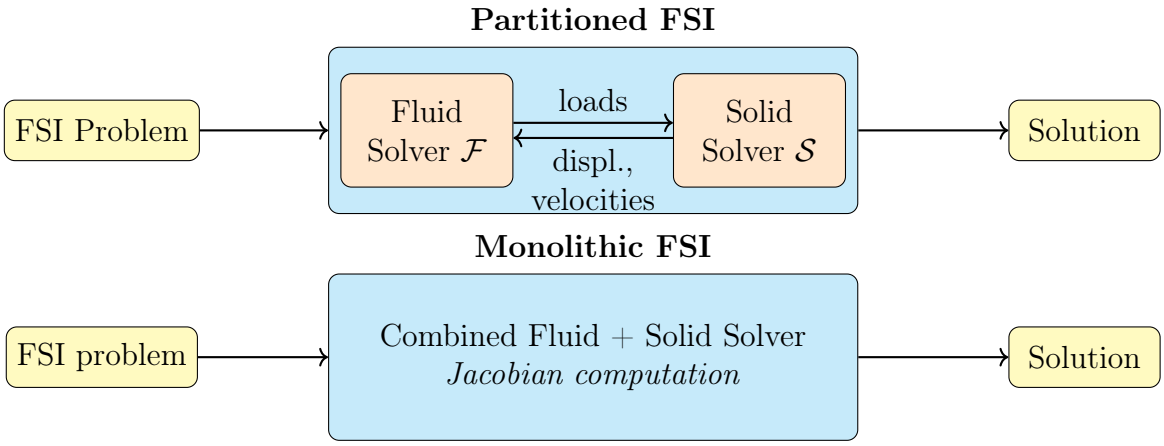


Figure 4.1: Comparison between partitioned and monolithic approaches in fluid–structure interaction problems.

4.1.2 Added-Mass Effects

The coupling strategy may vary depending on the problem at hand. Despite their advantages, partitioned approaches are known to suffer from convergence and stability issues, particularly when the densities of the fluid and the solid are of the same order of magnitude. This issue is known as added-mass effects.

In fluid mechanics this term traditionally refers to the additional apparent inertia experienced by a body moving inside a fluid as a consequence of the fact that, by its motion, the body displaces some volume of surrounding fluid. However, in the context of FSI, the same term is also used to describe numerical instabilities arising from the coupling procedure. According to the literature, conditions favorable to the appearance of added-mass instabilities are solid-to-fluid density ratio close to or lower than one, the presence of slender and flexible structures and small time step sizes [4].

Beyond the added-mass effects, the stability of partitioned FSI methods is also influenced by numerical aspects such as the discretization of the governing equations, the choice of numerical schemes and the time step size. Furthermore, physical and modeling assumptions such as incompressibility, the fluid-to-solid density ratio, material properties, and boundary conditions significantly influence the overall stability of the coupled system. These factors are often interrelated [21].

4.1.3 Coupling Strategies

To address these instabilities, various coupling strategies have been developed in the literature. These include strong coupling algorithms such as the Interface Quasi-Newton Inverse Least Squares (IQN-ILS) method. This method improves convergence and mitigates added-mass effects. Other approaches rely on iterative schemes such as explicit or implicit Block Gauss–Seidel algorithms. They can also be combined with relaxation techniques [4]. Additionally, acceleration methods such as the Aitken relaxation technique are widely used to enhance convergence rates [10]. Finally, algorithms such as the Gravouil–Combescure (GC) method provide alternative strategies for stabilizing the coupling between fluid and structure solvers [22].

In partitioned FSI approaches, different numerical methods are used to solve each physical domain. Computational Fluid Dynamics (CFD) methods, typically based on an Eulerian framework, are commonly employed to model fluid flows, while the Finite Element Method (FEM) is widely used in solid mechanics. However, when dealing with more complex flows involving large deformation, free surfaces or complex interface evolution, classical Eulerian CFD approaches may become limited due to mesh distortion and difficulties in accurately capturing moving boundaries and interfaces. To overcome these limitations, the fluid domain is solved here with PFEM (Chapter 2).

4.2 Simulation 2 — Buoyancy-Driven Dynamics

4.2.1 Problem Setup

Objective

The objective of this second simulation is to move from a kinematically driven gate to a dynamically driven one. The motion should emerge from a torque balance rather than being prescribed.

The dynamic coupling is first assessed using a simple constant driving torque, before adopting a physically grounded mechanism representative of the actual MOSE actuation.

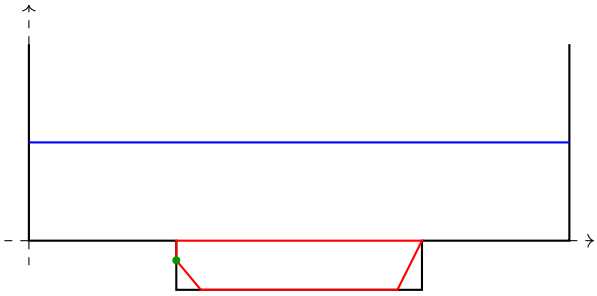


Figure 4.2: Initial Configuration

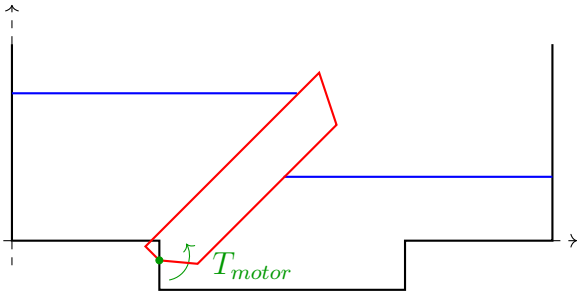


Figure 4.3: Rotated Configuration

Governing Equations of the Solid Body

The motion of the rigid body is described as a combination of translation and rotation about its center of mass.

The translational dynamics are governed by Newton's second law:

$$\sum \mathbf{F}(t) = m\,\mathbf{a}(t) \tag{4.3}$$

with m the mass of a MOSE gate [kg] and $\mathbf{a}$ the acceleration [m/s^2]. The rotational dynamics are given by:

$$\sum \mathbf{T}(t) = I\,\ddot{\theta}(t) \tag{4.4}$$

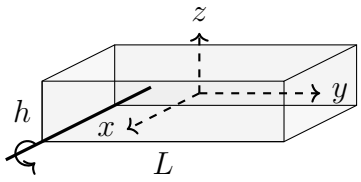
where I is the moment of inertia [kg·m^2] defined below, and $\ddot{\theta}$ is the angular acceleration of a gate [rad/s^2] .

The total resulting torque about the hinge gathers three contributions:

- T_{hydro} : The hydrodynamic torque exerted by the fluid pressure and viscous stresses on the wetted boundary. It also includes buoyancy.
- $T_{gravity}$: The gravitational torque associated with the weight of the structure
- T_{motor} : The motor torque, externally applied.
  As detailed below, the driving of the gate is realized in two successive steps. First, through a constant motor torque used to probe the dynamic coupling. Then through a variation of the effective density that modulates $T_{gravity}$ and reproduces the buoyancy-driven actuation of the real system.

In a more advanced model, additional terms such as a damping and a restoring torque could be included to stabilize the system around a given equilibrium position.

The moment of inertia of the barrier plays a key role in its dynamic response. It is computed based on the geometry and mass distribution of the structure.



$$I = \frac{1}{12}M(L^2 + h^2) + Md^2 \qquad (4.5)$$

where $I_x = \frac{1}{12}M(L^2 + h^2)$ is the moment of inertia about the centroidal axis and Md^2 is the contribution of the parallel axis theorem, with d the distance between the rotation axis and the center of mass and M, the total mass of the rigid body.

Simulation Parameters

Parameter	**Symbol**	**Value**	**Unit**
Initial angle	θ_0	$\pi/10$	rad
Maximum velocity	$v_{\max}$	$2\omega L_{mose}$	m/s
Time step	Δt	0.1 s_{min}/v_{max}	s

Boundary	**Condition**
Vertical walls	Free slip $\mathbf{u} \cdot \hat{\mathbf{n}} = 0$
Bubble	$\boldsymbol{\sigma} \cdot \hat{\mathbf{n}} = p_{\text{cavity}}\hat{\mathbf{n}}$

Table 4.1: Simulation 2 parameters and common boundary conditions (all other parameters as in Table 3.2).

4.2.2 First Attempt : Constant Motor Torque

Starting from the previous simulation framework and modifying the activation mechanism of the barrier motion (i.e. replacing the imposed displacement with a motor torque and accounting for inertia), the following observations can be made.

The system exhibits a strong sensitivity to both the applied torque and the moment of inertia. Even for moderate values, the angular velocity rapidly becomes excessively large, leading to divergence of the solution. Small variations in these parameters result in significantly different behaviors, making the calibration of the motor torque particularly challenging.

Diagnostic

These instabilities can be attributed to two main factors:

- The explicit Fluid-Structure Interaction (FSI) coupling,
- Inaccuracies in boundary detection within the PFEM framework.

In order to address these issues, a simplified geometry was considered. The system reduces to a rectangular barrier without a sill recess. This choice allows for a clearer understanding of the underlying mechanisms. It provides a suitable framework for implementing and validating the two solutions outlined below.

FSI Coupling

The explicit coupling between the fluid and the solid leads to numerical instabilities for the considered time steps. In particular, the direct use of computed forces and torques results in large oscillations and divergence of the solution. A relaxation technique is therefore introduced. The temporal evolution of the solid acceleration is updated as a combination of its current and previous values:

Let $\Delta\mathbf{v}^n$ and $\Delta\omega^n$ denote the translational and angular accelerations computed at time step n. The relaxed quantities are defined as:

$$\begin{aligned} \Delta\mathbf{v}^n_{\text{relaxed}} &= (1-\alpha)\,\Delta\mathbf{v}^{n-1}_{\text{relaxed}} + \alpha\,\Delta\mathbf{v}^n, \\ \Delta\omega^n_{\text{relaxed}} &= (1-\alpha)\,\Delta\omega^{n-1}_{\text{relaxed}} + \alpha\,\Delta\omega^n \end{aligned} \tag{4.6}$$

where $\alpha \in [0,1]$ is the relaxation coefficient. A small value of α increases stability

by damping rapid variations, at the cost of a slower response of the system. In this case, the relaxation coefficient is `alpha_relax` = 0.1. Aitken's adaptive relaxation was also tested but did not yield a significant stability improvement in the present configuration.

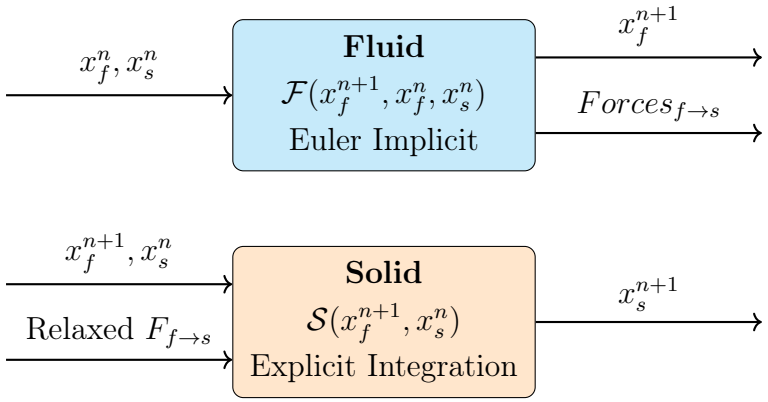


Figure 4.4: Fluid–solid coupling scheme: implicit fluid solve and explicit solid update through exchanged interaction forces.

The resulting coupling scheme is illustrated in Fig. 4.4. At each time step, the fluid solver $\mathcal{F}$ advances implicitly using the fluid and solid states at time n, producing the updated fluid state x_f^{n+1} and the fluid-to-solid interaction forces. Rather than being passed directly to the solid, these forces are relaxed according to the scheme above and transmitted to the solid solver $\mathcal{S}$. Then, $\mathcal{S}$ advances explicitly to yield x_s^{n+1}. The two subsystems thus exchange information sequentially within each time step.

Boundaries Detection

As explained in Chapter 2, the PFEM framework uses an alpha-shape algorithm to reconstruct the fluid domain at each time step. In the original implementation, boundary detection relied on the standard coloring procedure of the framework. However, this approach presented limitations in certain configurations. For example, narrow angles at solid boundaries could also make boundary detection more difficult. Additionally, bubbles forming along the barrier interface were not always properly detected and could persist artificially, polluting the solution.

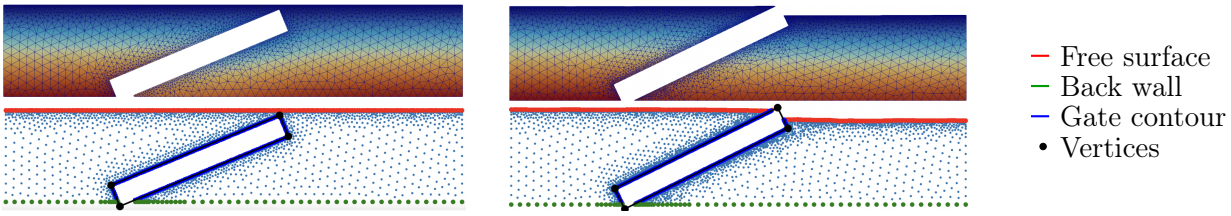


Figure 4.5: Simplified system at $t = 0.25\,\mathrm{s}$ (left) and $t = 50\,\mathrm{s}$ (right).

To address this, a manual boundary detection strategy was introduced. Each fluid node is assigned to a boundary if its distance to that segment falls below a prescribed tolerance `detect_tol`. This approach allows a more robust and explicit control over boundary assignment.

However, the tolerance must be chosen carefully. A value too small causes corner nodes (located at the intersection of two boundary segments) to remain unassigned. This introduces spurious pressure jumps at the corners of the barrier. A value too large risks misassigning nodes to the wrong boundary. The value `detect_tol` $= 1 \times 10^{-1}$ was retained as a compromise, smaller than the minimum mesh size $s_{\min}$ to avoid misassignments, yet large enough to capture corner nodes reliably.

4.2.3 Buoyancy-Driven Configuration

The constant motor torque is replaced by a driving mechanism representative of the real MOSE actuation.

The air injection mechanism is simulated by a time-varying effective density ρ_{eff} of the gate. Initially ρ_{eff} equals water density because the gate is filled with water. As air replaces the water filling the structure, ρ_{eff} decreases to reach ρ_{empty} (see Tab 4.2).

This reduction lowers the weight torque T_{gravity}, while the upward hydrodynamic torque persists. When the latter exceeds the former, the net torque becomes positive and lifts the gate. The motion of the structure therefore emerges from the balance between T_{gravity}, T_{hydro} and the inertia of the body.

In practice, the effective density is ramped from ρ_{full} to ρ_{empty} over the emptying interval $[t_{start}, t_{empty}]$ using a smooth-step profile. The smooth-step $\alpha(\tau) = 3\tau^2 - 2\tau^3$ has zero slope at both ends, so the weight torque varies smoothly.

The value of ρ_{empty} was estimated from gate geometry, by dividing the mass of an empty gate by the volume of a Lido-inlet gate.

Additional Simulation Parameters

Parameter	Symbol	Value	Unit
Gate opening start time	t_{start}	1	s
Gate draining duration	t_{empty}	30	s
Gate initial effective density	ρ_{full}	1000	kg/m^3
Gate final effective density	ρ_{empty}	125	kg/m^3

Table 4.2: Simulation 2 additional parameters

4.2.4 Second Attempt : Buoyancy-Driven Torque

The buoyancy-driven torque is now applied, together with the relaxation and boundary-detection corrections introduced above. The resulting torques are shown in Figure 4.6. Up to about $t = 24$ s, the solution evolves consistently with the expected physics. Around $t = 25$ s, however, it diverges before the gate has reached equilibrium ($T_{net} = 0$).

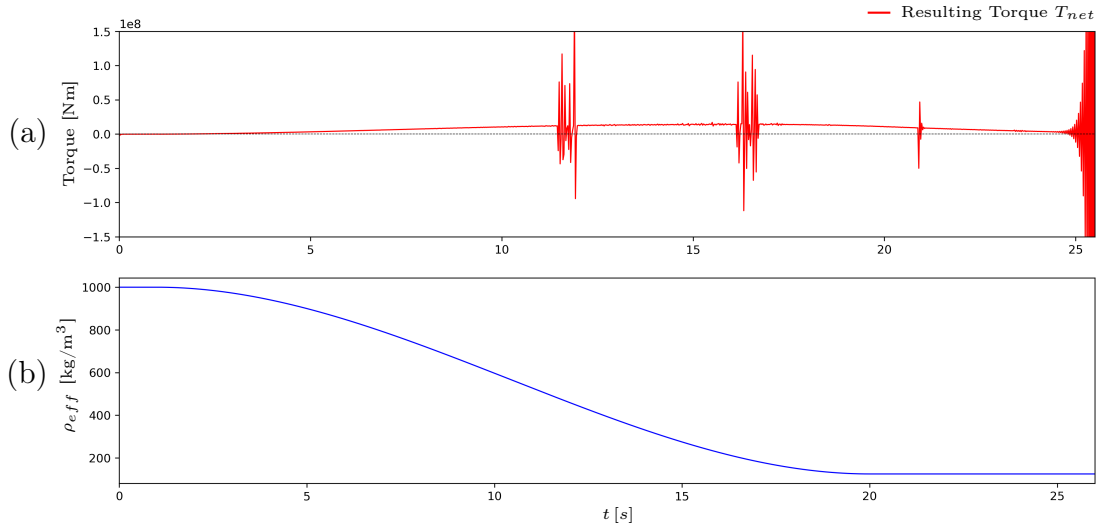


Figure 4.6: (a) Resulting torque acting on the barrier as a function of time. (b) Effective density of the MOSE barrier as a function of time.

Diagnostic

By that time, the effective density has dropped close to ρ_{empty}. The solid-to-fluid density ratio has fallen below about 0.2. This is the regime identified in Section 4.1.2 as prone to added-mass instabilities. It is similar to the explicit-coupling weakness as before but in its added-mass-dominated form. As the gate becomes very light, its physical inertia is too small for the explicit update and the relaxation alone is no longer sufficient to keep the solution stable.

Added-Mass Correction

The added-mass effect is incorporated implicitly in the solid update following the strategy of Section 4.1.2. The inertia entering the angular momentum balance is augmented by an added-mass contribution, estimated from the displaced fluid volume:

$$I_{\text{eff}} = I(m_{mose}) + I(m_{added}), \qquad m_{mose} = \rho_{\text{eff}}\, V_{mose}, \quad m_{added} = C_m\, \rho_f\, V_{mose} \tag{4.7}$$

with I(m) defined by Eq. 4.5, the parallel-axis inertia of a mass m about the hinge, C_m the added-mass coefficient ($C_m = 1$, a conservative estimate), ρ_f the fluid density and V_{mose} the gate volume. The corresponding results are presented in the next section.

4.2.5 Results

Torque Balance and Effective Density

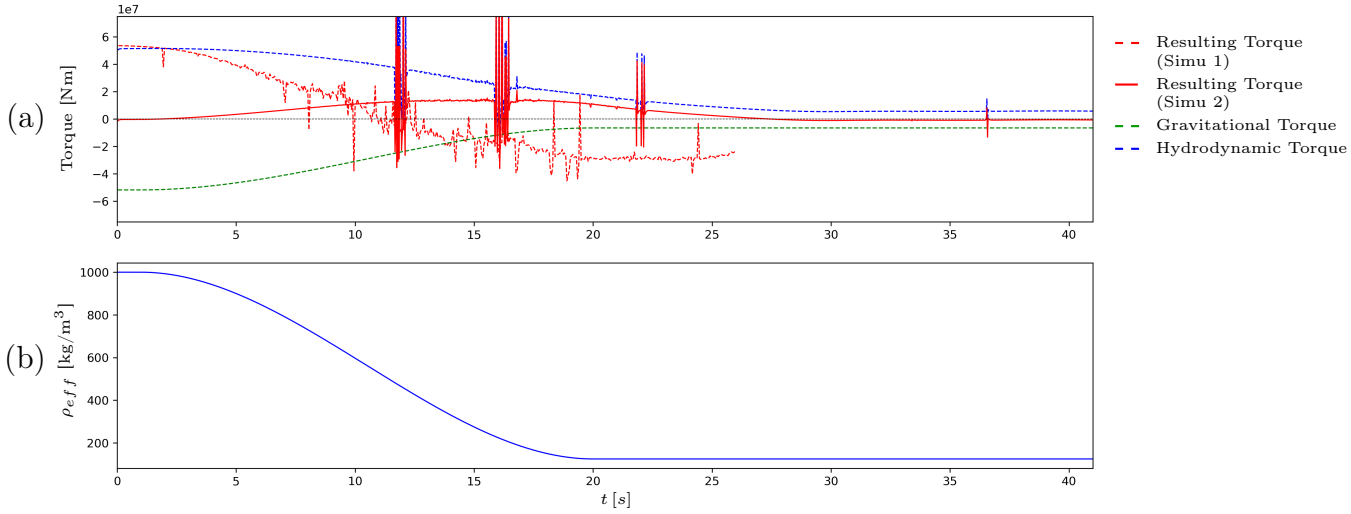


Figure 4.7: (a) Torques acting on the barrier as a function of time. (b) Effective density of the MOSE barrier as a function of time.

Figure 4.7(a) shows the time evolution of the torques acting on the gate. The dynamic formulation makes the sign of the resulting torque more intuitive than in Simulation 1. A zero resultant corresponds to rest or equilibrium, a positive resultant drives the gate counterclockwise (rising), and a negative resultant drives it clockwise (lowering).

The fluid-induced torque initially matches the value obtained in Simulation 1, as both cases start from the same configuration with the fluid at rest. The two curves then diverge. In Simulation 2 the hydrodynamic torque decreases toward zero whereas in Simulation 1 it becomes negative and remains significant. This difference reflects the nature of the motion. In Simulation 1 the imposed rotation continuously forces the fluid, which never reaches equilibrium. The hydrodynamic torque reflects this resistance. It opposes the prescribed rise and gives a sustained negative value. In Simulation 2 the gate moves freely and slowly, decelerating as it approaches equilibrium. As the angular velocity vanishes, the dynamic contribution disappears and only the quasi-static (buoyancy) part remains. At equilibrium it balances the now small weight torque of the nearly air-filled gate, so both tend toward zero.

As the effective density decreases (Figure 4.7(b)), the balance shifts progressively

from a net zero torque at the beginning of the simulation to a net upward torque, which sets the gate in motion, and again tends to 0 as the gate progressively reaches equilibrium.

A few large oscillations appear at some instants. They are likely caused by a node being assigned to the wrong boundary and that triggers a local instability before the solution recovers. Further tuning of the time step or the detection tolerance could probably reduce them.

Angular Response

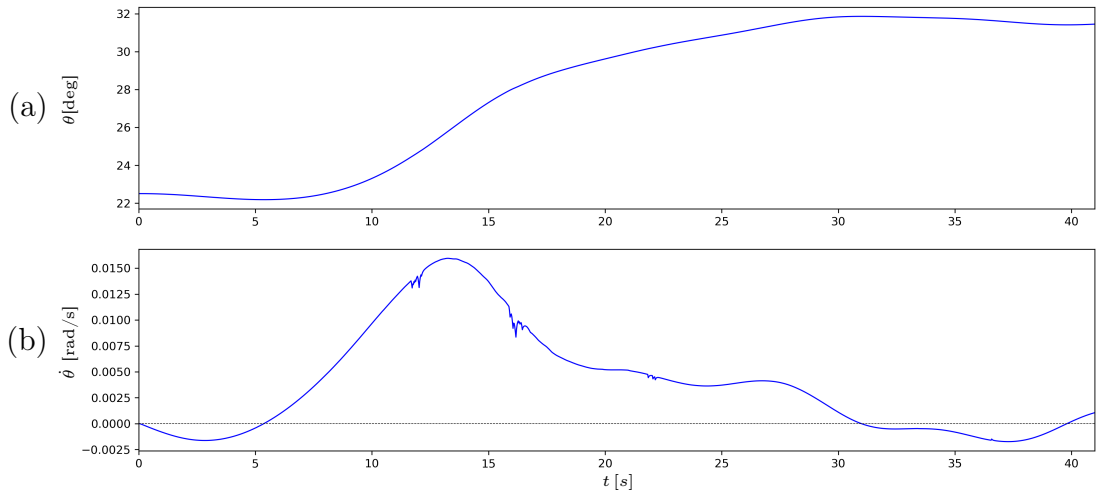


Figure 4.8: (a) Angular position of the mose system as a function of time. (b) Angular velocity as a function of time

Figure 4.8(b) shows that the response of the system remains close to the progressive (Gaussian) velocity profile imposed in Simulation 1. There are two notable differences. First, the angular velocity reached during the rise remains much lower than the value imposed in Simulation 1. Second, the gate begins by descending slightly before rising. It means that at early times the effective density is still high enough for the weight torque to exceed the hydrodynamic torque.

The angle stabilizes around 32°. This corresponds to the equilibrium configuration where the net torque tends to zero.

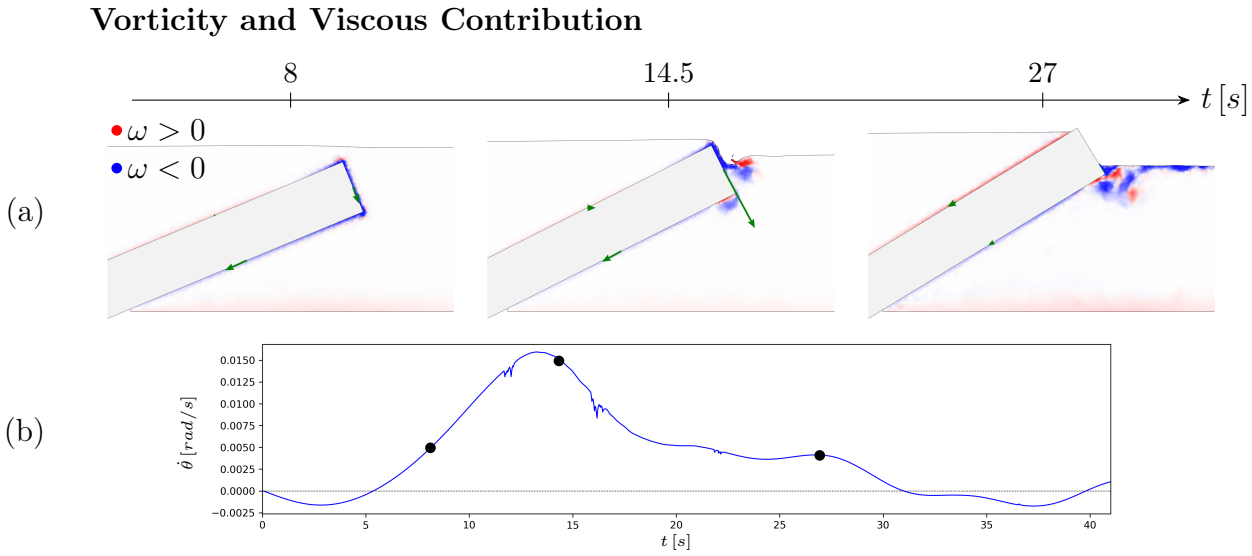


Figure 4.9: Snapshots of the barrier at different times for the Gaussian angular velocity profile. (a) Viscous force resultant per face and vorticity field. (b) Angular velocity profile with markers indicating the snapshot instants.

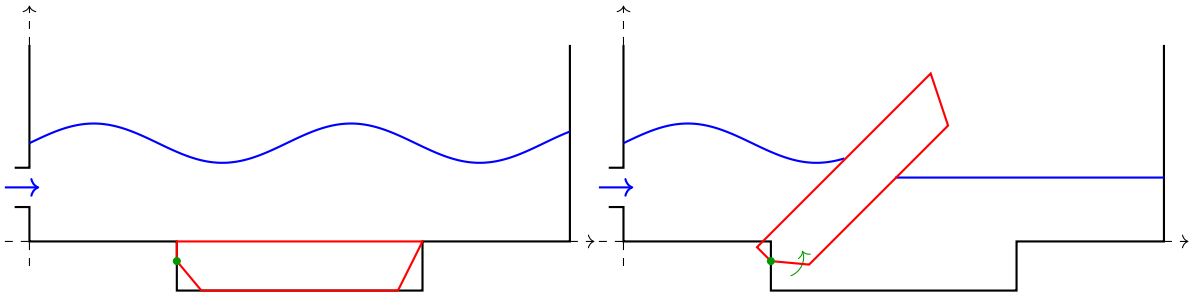
The pressure distribution remains similar to Simulation 1, as it is hydrostatically dominated. As visible on Figure 4.9, the viscous response differs. The gate is much slower so the viscous forces are even smaller, and the vorticity stays attached to the walls, without the separation or recirculation observed in Simulation 1.

4.3 Simulation 3 — Wave Interaction

4.3.1 Problem Setup

Objective

Simulation 3 extends the coupled configuration of Simulation 2 by subjecting the gate to an incoming wave. The aim is to observe the interaction between a wave and the deploying barrier. It represents a loading closer to the conditions the MOSE encounters during a storm surge. The configuration builds directly on Simulation 2 and modifies only the inlet boundaries.



Initial Configuration Rotated Configuration

Boundary Conditions

The wave is introduced through a Dirichlet velocity condition on the left wall.

A first attempt imposed a uniform inflow over the whole water column. Water then piled up against the gate, which lifted but was quickly submerged since no outflow let the excess escape. Such an outflow is usually provided by a free-pressure condition ($p = 0$) on the opposite wall. Here, however, the gate blocks the flow and the downstream side receives no continuous supply, so $p = 0$ simply drains it.

The right wall is therefore kept closed, and the inflow is made zero-mean and oscillating:

$$u_{\text{in}}(t) = A \sin\left(\frac{2\pi t}{T_{\text{wave}}}\right). \tag{4.8}$$

Because the sine averages to zero over a period, no net mass enters the domain. The mean water level stays constant while waves propagate toward the gate.

Simulation Parameters

Parameter	Symbol	Value	Unit
Wave Amplitude	A_1	1	m/s
Wave Amplitude	A_2	3	m/s
Wave Period	T_{wave}	6	s

Boundary	Condition
Right Vertical wall	Free slip $\mathbf{u} \cdot \hat{\mathbf{n}} = 0$
Left Vertical wall	Dirichlet Condition $\mathbf{u} = A \sin(2\pi\, t/T_{wave})$
Bubble	$\boldsymbol{\sigma} \cdot \hat{\mathbf{n}} = p_{\text{cavity}} \hat{\mathbf{n}}$

Table 4.3: Simulation 3 parameters and common boundary conditions (all other parameters as in Table 3.2).

4.3.2 Results

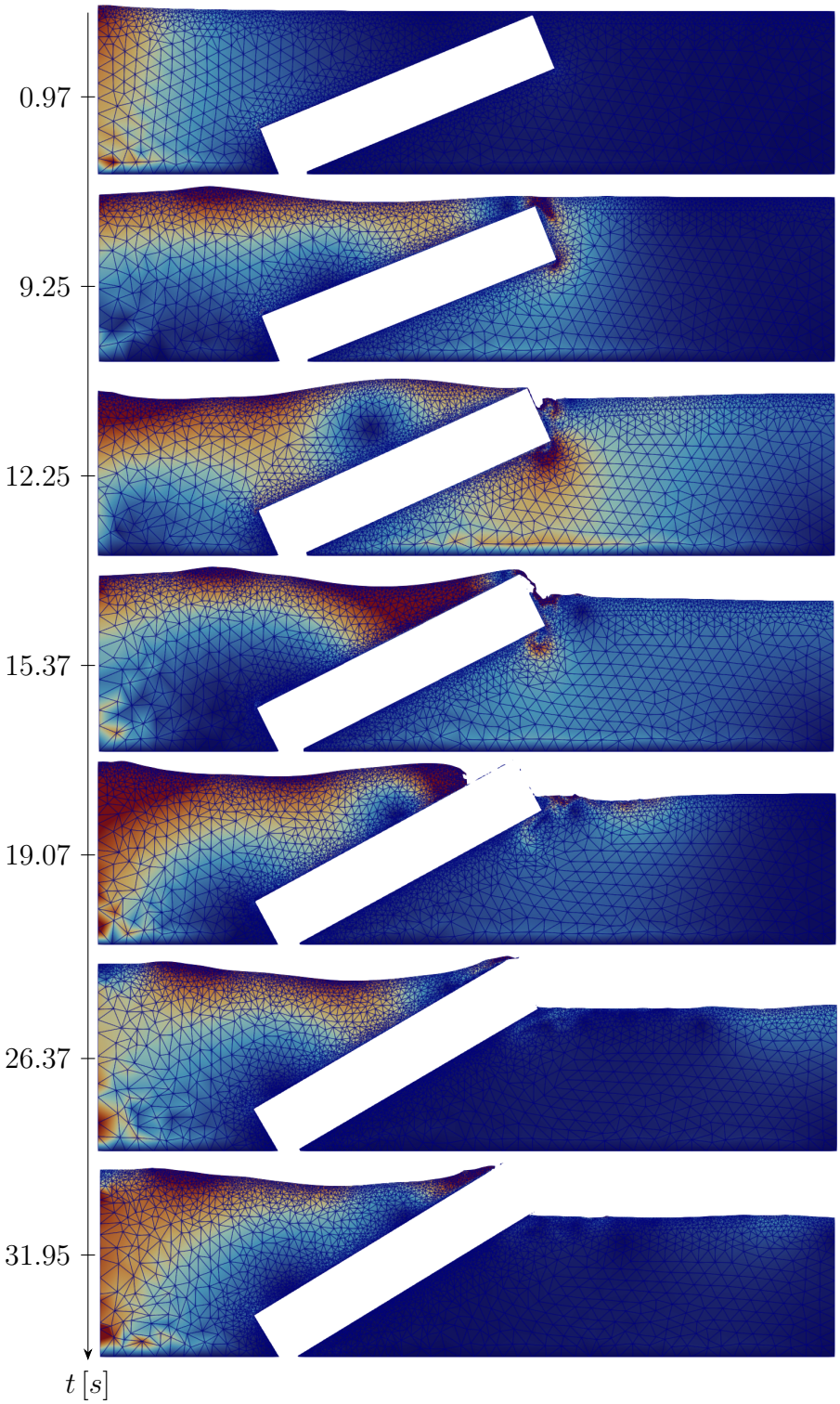


Figure 4.10: Snapshots of the velocity magnitude (0–1.5m/s).

Figure 4.10 shows the incoming wave reaching the structure at successive instants.

The torque response (Figure 4.11) is comparable to that of Simulation 2, both in order of magnitude and in the way it stabilizes. This is consistent with the torque being dominated by hydrostatic pressure. The wave superimposes only a small dynamic perturbation on it. The larger wave amplitude makes the wave signature more visible. The hydrodynamic torque keeps oscillating and the resulting torque follows as the weight torque is constant after 20s.

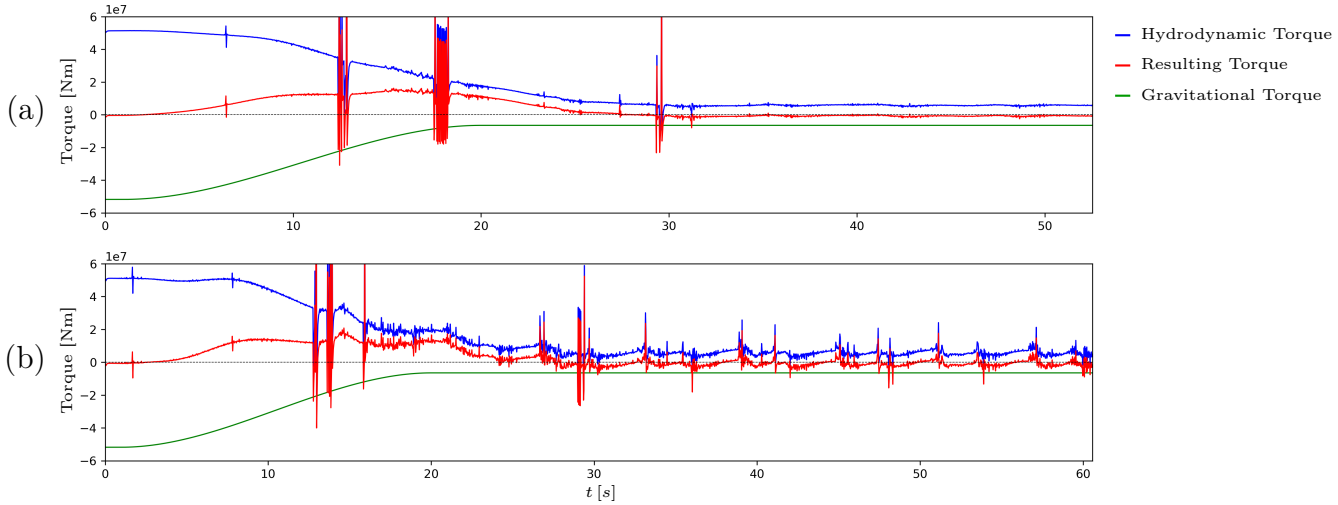


Figure 4.11: Torques acting on the barrier as a function of time for $A_1 = 1$ m/s (a) and for $A_2 = 3$ m/s (b).

The most noticeable difference lies in the angular response. For the amplitude A_1, Figure 4.12(a) shows that the gate takes longer to settle around its equilibrium angle than in Simulation 2. For the larger amplitude, we can observe that the angle is oscillating around a mean value rather than reaching a static equilibrium.

The angular velocity (Figure 4.12(b)) exhibits clear oscillations, stronger at this larger amplitude. The first ones share the 6 s period of the incoming wave. The oscillation period then changes likely because of the superposition with the waves reflected back by the barrier.

Such a response is expected, since the sustained periodic forcing continuously perturbs the gate.

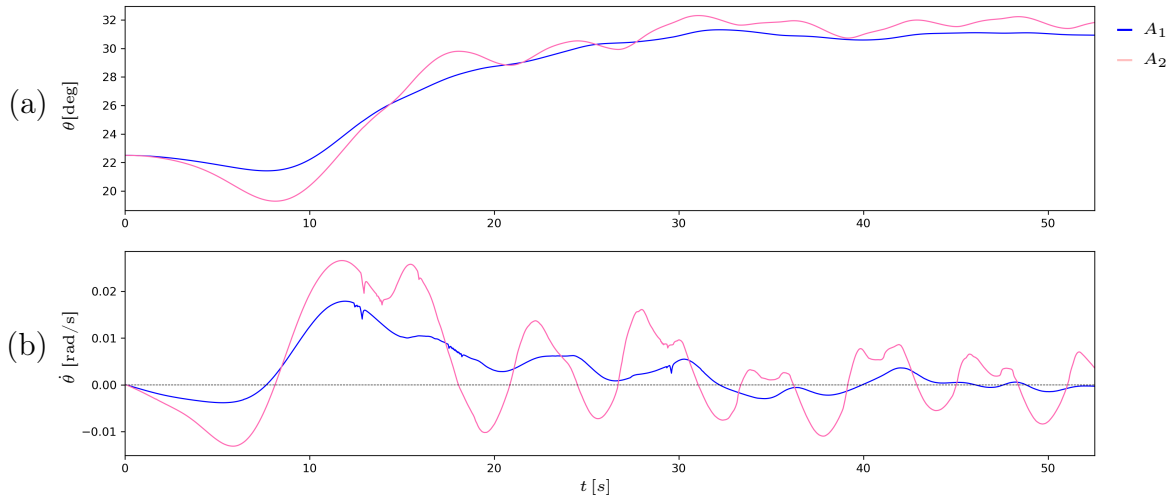


Figure 4.12: (a) Angular position of the mose system as a function of time. (b) Angular velocity as a function of time

These results remain preliminary and qualitative. The wavemaker is a simplified representation of a real wave field. Moreover, the forcing in the Venice lagoon is dominated by tides, whose periods are far longer ($\simeq 12h$). This is harder to reproduce at this scale. The results nonetheless show that the coupled PFEM model can handle a moving gate under wave loading and they open the way to a more detailed study of wave–barrier interaction.

Conclusion

Venice faces a steadily increasing flood risk, driven by the combined effect of land subsidence and a relative sea-level rise amplified by climate change. The growing frequency of *acqua alta* events led the city to deploy the MOSE system, a storm surge barrier made of bottom-hinged gates. These gates rest, water-filled, on the seabed under normal conditions. When a tide above the safeguarding threshold is forecast, compressed air replaces the water inside the gates, which then rotate upward and temporarily isolate the lagoon from the Adriatic Sea.

Within this context, the objective of this thesis was to develop a numerical model able to represent the fluid–structure interaction of a MOSE-inspired barrier using the Particle Finite Element Method (PFEM), with particular attention to the evolving free surface, the hydrodynamic loading on the gate, its large rotations, and the coupling between the fluid and the structure.

Chapter 1 laid the groundwork needed to understand the MOSE system. It presented the hydrodynamic processes in the lagoon that lead to *acqua alta*, the broader question of coastal flood mitigation, in particular the role of storm surge barriers for densely developed coastlines, and finally the operating principle of the MOSE barrier itself. Chapter 2 then introduced the theoretical and numerical framework of the PFEM, including domain detection through the α-shape, adaptive remeshing based on Delaunay triangulation, the resolution of the Navier–Stokes equations in a Lagrangian setting, and the stabilization required by equal-order P1/P1 elements.

Chapter 3 put the method into practice through a first simulation in which the gate motion was prescribed by an imposed angular velocity. This controlled setting served to characterize the hydrodynamic loads generated during the deployment of the barrier. Given the scale of the problem and the resulting high Reynolds number ($Re \simeq 10^7$), the pressure contribution proved to be largely dominant over the viscous one. A local analysis of the vorticity field nevertheless revealed flow separation and recirculation around the moving gate, with which the small viscous forces are closely correlated.

Chapter 4 extended this work to the fluid–structure interaction problem, moving from a kinematically prescribed motion to a dynamically driven gate. This coupling raised several numerical difficulties, which were addressed through a relaxation technique, a dedicated boundary-detection strategy, and an implicit added-mass cor-

rection that markedly improved stability. The resulting behaviour is more physically meaningful. The different contributions to the net torque can be followed individually, and the gate settles around an equilibrium angle of approximately 32° while its angular velocity oscillates around zero. Compared with the prescribed-motion case, the gate moves much more slowly, so that viscous effects are even weaker and no recirculation develops. A final simulation subjected the coupled gate to an incoming wave. These results remain preliminary and qualitative. The wavemaker is a simplified representation of a real wave field, and the forcing in the Venice lagoon is in practice dominated by tides, whose periods ($\simeq$ 12 h) are far longer and harder to reproduce at this scale. They nonetheless show that the coupled PFEM model can handle a moving gate under wave loading, and they open the way to a more detailed study of wave–barrier interaction.

Several limitations should be kept in mind when interpreting these results. The no-slip condition imposed on the gate, combined with the limited mesh resolution near its boundary, could introduce some uncertainty in the estimation of the viscous contribution. The two-dimensional assumption neglects three-dimensional effects, which may become significant near the gate edges. Finally, the wave forcing remains an idealized representation that does not capture the full complexity of the hydrodynamic conditions encountered by the real structure.

These limitations naturally point to several directions for future work. A three-dimensional extension would relax the planar assumption and allow end effects to be assessed. The partitioned coupling could also be compared with a monolithic formulation. Since the structure reduces to a single rigid body, the latter only adds one degree of freedom to the system and would be inherently robust to the added-mass instabilities encountered here. A sensitivity analysis on the wall treatment of the gate (no-slip versus free-slip) would help quantify the role of the tangential momentum transfer. Beyond the gate dynamics, the inclusion of sediment transport, only briefly touched upon in this work despite its importance for the lagoon, could be explored by leveraging the granular-flow capabilities of the *MigFlow* framework. Lastly, a quantitative validation against real prototype data, or against a reduced-scale physical experiment as reported in several PFEM studies, would be a valuable step toward a predictive model.

Bibliography

[1] Marlies H Barendrecht, Alberto Viglione, and Günter Blöschl. A dynamic framework for flood risk. *Water Security*, 1:3–11, 2017.

[2] Biodiversity Gateway. Salt marshes, 2024. Accessed: May 2026.

[3] Marco Lucio Cerquaglia, Geoffrey Deliége, Romain Boman, Vincent Terrapon, and Jean-Philippe Ponthot. Free-slip boundary conditions for simulating free-surface incompressible flows through the particle finite element method. *International Journal for numerical methods in engineering*, 110(10):921–946, 2017.

[4] Marco-Lucio Cerquaglia, David Thomas, Romain Boman, Vincent Terrapon, and J-P Ponthot. A fully partitioned lagrangian framework for FSI problems characterized by free surfaces, large solid deformations and displacements, and strong added-mass effects. *Computer Methods in Applied Mechanics and Engineering*, 348:409–442, 2019.

[5] Matthieu Constant, Frédéric Dubois, Jonathan Lambrechts, and Vincent Legat. Implementation of an unresolved stabilised fem–dem model to solve immersed granular flows. *Computational Particle Mechanics*, 6(2):213–226, 2019.

[6] Colin J Cotter, David A Ham, Christopher C Pain, and Sebastian Reich. LBB stability of a mixed galerkin finite element pair for fluid flow simulations. *Journal of Computational Physics*, 228(2):336–348, 2009.

[7] Massimiliano Cremonesi, Alessandro Franci, Sergio Idelsohn, and Eugenio Oñate. A state of the art review of the particle finite element method (PFEM) m. cremonesi et al. *Archives of Computational Methods in Engineering*, 27(5):1709–1735, 2020.

[8] Robert G Dean and Robert A Dalrymple. *Water wave mechanics for engineers and scientists*, volume 2. world scientific publishing company, 1991.

[9] Joris Degroote. Partitioned simulation of fluid-structure interaction: Coupling black-box solvers with quasi-newton techniques. *Archives of computational methods in engineering*, 20(3):185–238, 2013.

[10] Joris Degroote, Peter Bruggeman, Robby Haelterman, and Jan Vierendeels. Stability of a coupling technique for partitioned solvers in fsi applications. *Computers & Structures*, 86(23-24):2224–2234, 2008.

[11] H. Edelsbrunner, D. Kirkpatrick, and R. Seidel. On the shape of a set of points in the plane. *IEEE Transactions on information theory*, 29(4):551–559, 1983.

[12] Carlo Giupponi, Marco Bidoia, Margaretha Breil, Luca Di Corato, Animesh Kumar Gain, Veronica Leoni, Behnaz Minooei Fard, Raffaele Pesenti, and Georg Umgiesser. Boon and burden: economic performance and future perspectives of the venice flood protection system. *Regional environmental change*, 24(2):44, 2024.

[13] Charbel Habchi, Serge Russeil, Daniel Bougeard, Jean-Luc Harion, Thierry Lemenand, Akram Ghanem, Dominique Della Valle, and Hassan Peerhossaini. Partitioned solver for strongly coupled fluid–structure interaction. *Computers & Fluids*, 71:306–319, 2013.

[14] Michel Henry. *Numerical methods for granular media in multiphase fluids*. PhD thesis, UCL-Université Catholique de Louvain, 2025.

[15] J William Kamphuis. *Introduction to coastal engineering and management*, volume 48. World Scientific, 2020.

[16] Pijush K Kundu, Ira M Cohen, David R Dowling, and Jesse Capecelatro. *Fluid mechanics*. Elsevier, 2024.

[17] Martin Lacroix. *Robust PFEM-FEM Partitioned Coupling Framework for the Simulation of Solids Under Complex Flow-Induced Loads*. PhD thesis, Universite de Liege (Belgium), 2025.

[18] Thomas Leyssens, Michel Henry, Jonathan Lambrechts, and Jean-François Remacle. A delaunay refinement algorithm for the particle finite element method

applied to free surface flows. *International Journal for Numerical Methods in Engineering*, 125(18):e7554, 2024.

[19] Zhe Li, Julien Leduc, Jorge Nunez-Ramirez, Alain Combescure, and Jean-Christophe Marongiu. A non-intrusive partitioned approach to couple smoothed particle hydrodynamics and finite element methods for transient fluid-structure interaction problems with large interface motion. *Computational Mechanics*, 55(4):697–718, 2015.

[20] Piero Lionello, David Barriopedro, Christian Ferrarin, Robert J Nicholls, Mirko Orlic, Fabio Raicich, Marco Reale, Georg Umgiesser, Michalis Vousdoukas, and Davide Zanchettin. Extremes floods of venice: characteristics, dynamics, past and future evolution. *Natural Hazards and Earth System Sciences Discussions*, 2020:1–34, 2020.

[21] Johan Lorentzon and Johan Revstedt. On stability and relaxation techniques for partitioned fluid-structure interaction simulations. *Engineering Reports*, 4(10):e12514, 2022.

[22] Simone Meduri, Massimiliano Cremonesi, and Umberto Perego. A fully explicit fluid-structure interaction approach based on pfem and fem. In *PARTICLES V: proceedings of the V International Conference on Particle-Based Methods: fundamentals and applications*, pages 195–202. CIMNE, 2017.

[23] Riccardo Alvise Mel. Exploring the partial use of the Mo.S.E. system as effective adaptation to rising flood frequency of venice. *Natural Hazards and Earth System Sciences Discussions*, 2021:1–30, 2021.

[24] Frank Meulen, Stéphanie IJff, and Rien van Zetten. Nature-based solutions for coastal adaptation management, concepts and scope, an overview. *Nordic Journal of Botany*, 2023, 07 2022.

[25] Leslie Mooyaart, Sebastiaan Jonkman, Peter de Vries, Ad Van der Toorn, and Mathijs van Ledden. Storm surge barrier: Overview and design considerations. *Coastal Engineering Proceedings*, 1(34):45, 2014.

[26] Stefania Munaretto, Pier Vellinga, and Hilde Tobi. Flood protection in venice under conditions of sea-level rise: An analysis of institutional and technical measures. *Coastal Management*, 40(4):355–380, 2012.

[27] David Pugh, Philip L Woodworth, and Philip Woodworth. *Sea-level science: understanding tides, surges, tsunamis and mean sea-level changes*. Cambridge university press, 2014.

[28] Paolo Sammarco, Piera Fischione, Alessandro Romano, Giorgio Bellotti, and Sergio Dalla Villa. Prototype data analysis of the dynamics of the venice gate-barriers during an extreme storm event. *Coastal Engineering*, 194:104623, 2024.

[29] Jonathan Richard Shewchuk. Delaunay refinement algorithms for triangular mesh generation. *Computational geometry*, 22(1-3):21–74, 2002.

[30] P.E. Smith. 2 - types of marine concrete structures. In Mark G. Alexander, editor, *Marine Concrete Structures*, pages 17–64. Woodhead Publishing, 2016.

[31] Reshma Sunkur, Komali Kantamaneni, Chandradeo Bokhoree, and Shirish Ravan. Mangroves' role in supporting ecosystem-based techniques to reduce disaster risk and adapt to climate change: A review. *Journal of Sea Research*, 196:102449, 2023.

[32] Tayfun E Tezduyar, Sanjay Mittal, SE Ray, and Ron Shih. Incompressible flow computations with stabilized bilinear and linear equal-order-interpolation velocity-pressure elements. *Computer Methods in Applied Mechanics and Engineering*, 95(2):221–242, 1992.

[33] Sunke Trace-Kleeberg, Ivan D. Haigh, Marc Walraven, and Susan Gourvenec. How should storm surge barrier maintenance strategies be changed in light of sea-level rise? a case study. *Coastal Engineering*, 184:104336, 2023.

[34] Georg Umgiesser, Marco Bajo, Christian Ferrarin, Andrea Cucco, Piero Lionello, Davide Zanchettin, Alvise Papa, Alessandro Tosoni, Maurizio Ferla, Elisa Coraci, et al. The prediction of floods in venice: methods, models and uncertainty. *Natural Hazards and Earth System Sciences*, 21(8):2679–2704, 2021.

[35] A Van der Nat, P Vellinga, R Leemans, and E Van Slobbe. Ranking coastal flood protection designs from engineered to nature-based. *Ecological Engineering*, 87:80–90, 2016.

[36] Mark VanKoningsveld, Jan PM Mulder, Marcel JF Stive, L VanDerValk, and Arjan W VanDerWeck. Living with sea-level rise and climate change: a case study of the netherlands. *Journal of coastal research*, 24(2):367–379, 2008.

[37] Charles J. Vos. *The Thames Barrier*, pages 291–308. Springer Netherlands, Dordrecht, 2002.

[38] Davide Zanchettin, Sara Bruni, Fabio Raicich, Piero Lionello, Fanny Adloff, Alexey Androsov, Fabrizio Antonioli, Vincenzo Artale, Eugenio Carminati, Christian Ferrarin, et al. Sea-level rise in venice: historic and future trends. *Natural Hazards and Earth System Sciences*, 21(8):2643–2678, 2021.

UNIVERSITÉ CATHOLIQUE DE LOUVAIN
École polytechnique de Louvain
Rue Archimède, 1 bte L6.11.01, 1348 Louvain-la-Neuve, Belgique | **www.uclouvain.be/epl**